Physics and Astronomy Faculty Publications

Physics and Astronomy

10-21-2014

# The Bulge–Disc Decomposed Evolution of Massive Galaxies at 1 < z < 3 in CANDELS

V. A. Bruce
*University of Edinburgh, UK*

J. S. Dunlop
*University of Edinburgh, UK*

R. J. McLure
*University of Edinburgh, UK*

M. Cirasuolo
*University of Edinburgh, UK*

F. Buitrago
*University of Edinburgh, UK*

*See next page for additional authors*

**Right click to open a feedback form in a new tab to let us know how this document benefits you.**

Follow this and additional works at: https://uknowledge.uky.edu/physastron_facpub

Part of the Astrophysics and Astronomy Commons, and the Physics Commons

**Authors**

V. A. Bruce, J. S. Dunlop, R. J. McLure, M. Cirasuolo, F. Buitrago, R. A. A. Bowler, T. A. Targett, E. F. Bell, D. H. McIntosh, A. Dekel, S. M. Faber, H. C. Ferguson, N. A. Grogin, W. Hartley, Dale D. Kocevski, A. M. Koekemoer, D. C. Zoo, and E. J. McGrath

**The Bulge–Disc Decomposed Evolution of Massive Galaxies at 1 < $z$ < 3 in CANDELS**

# The bulge–disc decomposed evolution of massive galaxies at 1 < z < 3 in CANDELS

V. A. Bruce,[1]★ J. S. Dunlop,[1] R. J. McLure,[1] M. Cirasuolo,[1,2] F. Buitrago,[1]
R. A. A. Bowler,[1] T. A. Targett,[3] E. F. Bell,[4] D. H. McIntosh,[5] A. Dekel,[6]
S. M. Faber,[7] H. C. Ferguson,[8] N. A. Grogin,[8] W. Hartley,[9] D. D. Kocevski,[10]
A. M. Koekemoer,[8] D. C. Koo[7] and E. J. McGrath[11]

[1]SUPA† Institute for Astronomy, University of Edinburgh, Royal Observatory, Edinburgh EH9 3HJ, UK
[2]UK Astronomy Technology Centre, Science and Technology Facilities Council, Royal Observatory, Edinburgh EH9 3HJ, UK
[3]Department of Physics and Astronomy, Sonoma State University,1801 East Cotati Avenue, Rohnert Park, CA 94928-3609, USA
[4]Department of Astronomy, University of Michigan, Ann Arbor, MI 48109, USA
[5]Department of Physics & Astronomy, University of Missouri-Kansas City, 5110 Rockhill Road, Kansas City, MO 64110, USA
[6]Racah Institute of Physics, The Hebrew University, Jerusalem 91904, Israel
[7]UCO/Lick Observatory, Department of Astronomy and Astrophysics, University of California, Santa Cruz, CA 95064, USA
[8]Space Telescope Science Institute, 3700 San Martin Drive, Baltimore, MD 21218, USA
[9]ETH Zürich, Institut für Astronomie, HIT J 11.3, Wolfgang-Pauli-Str. 27, 8093 Zürich, Switzerland
[10]Department of Physics and Astronomy, University of Kentucky, Lexington, KY 40506, USA
[11]Department of Physics and Astronomy, Colby College, Waterville, ME 0490, USA

## ABSTRACT

We present the results of a new and improved study of the morphological and spectral evolution of massive galaxies over the redshift range 1 < z < 3. Our analysis is based on a bulge–disc decomposition of 396 galaxies with $M_* > 10^{11} \, M_\odot$ uncovered from the Cosmic Assembly Near-infrared Deep Extragalactic Legacy Survey (CANDELS) Wide Field Camera 3 (WFC3)/IR imaging within the Cosmological Evolution Survey (COSMOS) and UKIRT Infrared Deep Sky Survey (UKIDSS) UDS survey fields. We find that, by modelling the $H_{160}$ image of each galaxy with a combination of a de Vaucouleurs bulge (Sérsic index $n = 4$) and an exponential disc ($n = 1$), we can then lock all derived morphological parameters for the bulge and disc components, and successfully reproduce the shorter-wavelength $J_{125}$, $i_{814}$, $v_{606}$ HST images simply by floating the magnitudes of the two components. This then yields sub-divided four-band HST photometry for the bulge and disc components which, with no additional priors, is well described by spectrophotometric models of galaxy evolution. Armed with this information, we are able to properly determine the masses and star formation rates for the bulge and disc components, and find that: (i) from $z = 3$ to 1 the galaxies move from disc dominated to increasingly bulge dominated, but very few galaxies are pure bulges/ellipticals by $z = 1$; (ii) while most passive galaxies are bulge dominated, and most star-forming galaxies disc dominated, $18 \pm 5$ per cent of passive galaxies are disc dominated, and $11 \pm 3$ per cent of star-forming galaxies are bulge dominated, a result which needs to be explained by any model purporting to connect star formation quenching with morphological transformations; (iii) there exists a small but significant population of pure passive discs, which are generally flatter than their star-forming counterparts (whose axial ratio distribution peaks at $b/a \simeq 0.7$); (iv) flatter/larger discs re-emerge at the highest star formation rates, consistent with recent studies of sub-mm galaxies, and with the concept of a maximum surface density for star formation activity.

**Key words:** galaxies: elliptical and lenticular, cD – galaxies: evolution – galaxies: high-redshift – galaxies: spiral – galaxies: structure.

★ E-mail: vab@roe.ac.uk
† Scottish Universities Physics Alliance.

# 1 INTRODUCTION

Although detailed morphological studies of galaxies have been conducted since the 1920s, the underlying physical processes responsible for the formation and subsequent evolution of galaxy morphologies remain to be fully understood. In particular, it is still unclear how, or even if, transformations in morphology are linked to star formation history.

Locally, galaxy morphologies are complex, with high-resolution studies finding that disc-dominated galaxies often possess additional structure such as bars, and central cores with exponential, disc-like, profiles(classified as pseudo-bulges Kormendy & Kennicutt 2004) which are proposed to originate through secular processes. Despite this, the recent local population morphological studies conducted using Sloan Digital Sky Survey (SDSS) data, have revealed that the overall galaxy populations can still be broadly represented by two classes: bulge-dominated (e.g. elliptical) and disc-dominated (e.g. spiral) systems, with a strong colour bimodality comprising a prominent red sequence of bulge-dominated galaxies and a blue-cloud of disc-dominated galaxies (Baldry et al. 2004; Driver et al. 2006; Drory & Fisher 2007). However, in more recent years, these studies have also led to the discovery of a more puzzling population of blue bulges and red discs (Bamford et al. 2009; Masters et al. 2010). These blue bulges and red discs appear to be at odds with the merger-driven hierarchical evolution paradigm, where it is proposed that gas-poor major mergers at intermediate redshifts transform galaxies from disc to bulge-dominated systems (e.g. Robertson et al. 2006) while simultaneously quenching star formation. Thus, the prevalence of quenching via major mergers in comparison to alternative quenching mechanisms (e.g. Schawinski et al. 2014) and the role of S0 galaxies during these processes (e.g. Johnston, Aragon-Salamanca & Merrifield 2014) remains unclear.

Increasingly detailed morphological studies are now able to push further back in cosmic time, into the key cosmic epoch at $1 < z < 3$ where the star formation rate density of the Universe peaks. These studies have found evidence that, while the Hubble sequence is observed to already be in place at these high redshifts, a larger fraction of galaxies are disc-dominated or composite systems (van der Wel et al. 2011; Chevance et al. 2012; Buitrago et al. 2013b; McLure et al. 2013) and there is an increase in the fraction of visually disturbed morphologies (Mortlock et al. 2013). In addition, disc structures are also observed to be 'clumpier' (Wuyts et al. 2012; Mozena et al., in preparation) and 'puffier' (Förster Schreiber et al. 2009). Intriguingly, the presence of passive discs has also been observed at higher redshifts ($z > 1$) (e.g. McGrath et al. 2008; Stockton et al. 2008; Cameron et al. 2011; van der Wel et al. 2011; McLure et al. 2013), providing further evidence that the physical processes which quench star formation may be distinct from those that drive morphological transformations.

Several of the currently proposed quenching mechanisms can account for the cessation of star formation and the retention of a massive disc, or the presence of star-forming bulges, including: models of violent disc instabilities (VDI; e.g. Dekel, Sari & Ceverino 2009b; Dekel & Burkert 2014), the 'hot halo' quenching scenario (e.g. Dekel et al. 2009a) new observational evidence for which has been reported recently by Hartley et al. (2013), and potentially the phenomenological mass and environment models of Peng et al. (2010b), where new evidence suggests that both of these processes may act on galaxy morphologies in the same way (Carollo et al. 2014). However, as yet, it is unclear which of these or which combination of these processes is most viable. In fact, recent focus has been placed on explicitly exploring the role that $B/T$ light and

mass fractions play in quenching fractions using both parametric (e.g. Bell et al. 2012) and non-parametric analyses (e.g. Cheung et al. 2012; Fang et al. 2013). The recent local study of Bluck et al. (2014) finds evidence for a link between passivity and bulge mass, and the study by Omand, Balogh & Poggianti (2014) suggests that the quenching fraction of central galaxies is not simply dependent on stellar mass but is also strongly correlated with $B/T$ fractions such that in the stellar mass range $9 < \log_{10}(M_*/M_\odot) < 11.5$ almost all galaxies with $B/T > 0.3$ are quenched. This connection between quiescence and $B/T$ fraction has also been observed by Lang et al. (2014) at $z \sim 2.5$ using both light and mass fractions from decompositions conducted in a similar manner to those presented in Bruce et al. (2012), and is consistent with both the VDI model of Dekel et al. (2009b) and Ceverino, Dekel & Bournaud (2010) and, given the natural connection between central bulge and black hole growth, AGN feedback. Within the context of these large statistical studies the role of the sub-dominant populations of passive discs and star-forming bulges is particularly interesting, as it is within the $1 < z < 3$ redshift range that we see a considerable build-up of the red sequence and observe galaxies undergoing significant morphological transformations. Therefore, further study of this informative regime is crucial for improving our understanding of the main drivers of galaxy morphology evolution and the processes responsible for star formation quenching.

In order to best conduct studies of the morphological evolution of galaxies at these redshifts, it is instructive to decompose the galaxies into their bulge and disc components. Bulge–disc decompositions have been conducted extensively in the local Universe (e.g. de Jong 1996; Allen et al. 2006; Cameron et al. 2009; Simard et al. 2011; Lackner & Gunn 2012), however Bruce et al. (2012) was the first study to attempt bulge–disc decomposition in the redshift range $1 < z < 3$ for a large sample (by utilizing the latest high-resolution imaging from *HST* Wide Field Camera 3 (WFC3) provided by the Cosmic Assembly Near-infrared Deep Extragalactic Legacy Survey (CANDELS) survey in the UDS field). In this paper, we further develop this work by effectively doubling the sample size [by including an analysis of the CANDELS Cosmological Evolution Survey (COSMOS) field], and extending the multiple-component analysis to the additional $J_{125}$, $i_{814}$ and $v_{606}$ bands provided by the CANDELS survey. Crucially, this has allowed us to construct separate bulge and disc model photometry across four bands, which has then enabled us to successfully isolate and model the spectral energy distributions (SEDs) of the bulge and disc components. The new multiple-component SED-fitting technique presented in this paper yields separate stellar mass estimates and star formation rates for the bulge and disc components of the massive galaxies within our sample. This has then enabled new exploration of the extent to which morphological transformations are linked to star formation quenching. Particular emphasis has been placed on addressing the dominance of the bulge and disc masses, the star formation activity displayed by the individual components, and the axial ratio distributions of the bulge and disc components.

This paper is structured as follows. In Section 2, we summarize our data sets and sample properties obtained from SED fitting. This is followed in Section 3 by a description of our multiple-component, multiwavelength, morphology-fitting technique, alongside which we present the results from our mock galaxy simulations, and discuss the extension to decomposed SED fitting in Section 4. In Section 5, we utilize our decomposed morphology and stellar mass results to explore the overall morphological evolution of the galaxies in our $1 < z < 3$ sample and in Section 6, we additionally incorporate the decomposed star formation rates of these objects

to study the links between morphology and star formation history, which includes a revised, stricter, identification of a population of passive discs and star-forming bulges. Section 7 focuses on a study of the axial ratios of our sub-divided galaxy sample and in Section 8, we extend this work to a comparison with (sub-)mm selected galaxies. Finally, we conclude with a discussion of the results from our decompositions within the context of current models of galaxy evolution and quenching and summarize our conclusions in Sections 9 and 10.

Throughout we quote magnitudes in the AB system, and calculate all physical quantities assuming a $\Lambda$ cold dark matter ($\Lambda$CDM) universe with $\Omega_{\rm m} = 0.3$, $\Omega_\Lambda = 0.7$ and $H_0 = 70\,{\rm km\,s^{-1}\,Mpc^{-1}}$.

## 2 DATA AND SAMPLE PROPERTIES

We have used the *HST* WFC3/IR data from the CANDELS multicycle treasury programme (Grogin et al. 2011; Koekemoer et al. 2011) centred on the UKIRT Infrared Deep Sky Survey (UKIDSS) Ultra Deep Survey (UDS; Lawrence et al. 2007) and COSMOS (Scoville et al. 2007) fields. Both the CANDELS UDS and COSMOS near-infrared data comprise $4 \times 11$ WFC3/IR tiles covering a total area of 187 arcmin$^2$ in each field, in both the *F125W* and *F160W* filters. The point source depths are 27.1 and 27.0 (AB mag, $5\sigma$) for the UDS and COSMOS fields, respectively. In addition to the near-infrared data, for this extended analysis, we have also made use of the accompanying CANDELS *HST* Advanced Camera for Surveys (ACS) parallel imaging in the *F814W* and *F606W* filters (hereafter $i_{814}$ and $v_{606}$). The corresponding $5\sigma$ point source depths are 28.4 for both the $i_{814}$ and $v_{606}$ bands in UDS and 28.5 in COSMOS, due to the inclusion of existing ACS legacy data in COSMOS (Koekemoer et al. 2007; Scoville et al. 2007). The WFC3 and ACS cameras are offset by 6 arcmin in the *HST* focal plane and during the CANDELS observations were oriented to provide the maximum area of contiguous WFC3+ACS coverage (which is ~80 per cent of the area of both fields).

### 2.1 Supporting multiwavelength data

In order to constrain the SED fitting and determine the physical properties for the galaxies in our sample, we have also utilized the multiwavelength data sets available in each field. In the UDS these comprise: $u'$-band imaging obtained with Mega-Cam on Canada France Hawaii Telescope (CFHT); deep optical imaging in the *B*, *V*, *R*, $i'$ and $z'$-band filters from the Subaru *XMM–Newton* Deep Survey (Sekiguchi et al. 2005; Furusawa et al. 2008); *J*, *H* and *K*-band UKIRT WFCAM imaging from Data Release 8 (DR8) of the UKIDSS UDS; and *Spitzer* 3.6 μm, 4.5 μm IRAC and 24 μm MIPS imaging from the SpUDS legacy programme (PI Dunlop). For COSMOS we use: optical imaging in $u'$, $g'$, $r'$, $i'$ and $z'$ bands from MegaCam CFHTLS-D2; $z'$ band from Subaru; *Y*, *J*, *H* and *K*s from UltraVISTA (PI Dunlop); and *Spitzer* 3.6 μm, 4.5 μm IRAC and 24 μm MIPS imaging from the S-COSMOS survey (PI Sanders).

### 2.2 Mass estimation and sample selection

We follow the same sample selection procedure detailed in Bruce et al. (2012) and have determined photometric redshifts for the UDS and COSMOS master samples using a $\chi^2$-fitting procedure based on the photometric-redshift code HYPERZ from Bolzonella, Miralles & Pelló (2000), described in Cirasuolo et al. (2007). These photometric redshifts were then used to determine stellar mass estimates; however in comparison to Bruce et al. (2012), we now implement a slightly updated stellar mass SED-fitting procedure which we have applied to the COSMOS field and have used to re-define the Bruce et al. (2012) UDS sample. These stellar mass estimates were based on the Bruzual & Charlot (2003) models with single-component exponentially decaying star formation histories with $e$-folding times in the range $0.3 \le \tau\,({\rm Gyr}) \le 5$ and with a minimum model age limit of 50 Myr to ensure physically meaningful mass estimates. This results in a sample of 205 objects in the UDS and 191 objects in COSMOS with $M_* > 1 \times 10^{11}\,{\rm M}_\odot$ in the $1 < z < 3$ redshift range, where this mass cut (corresponding to $H_{160} = 24.5$) provides
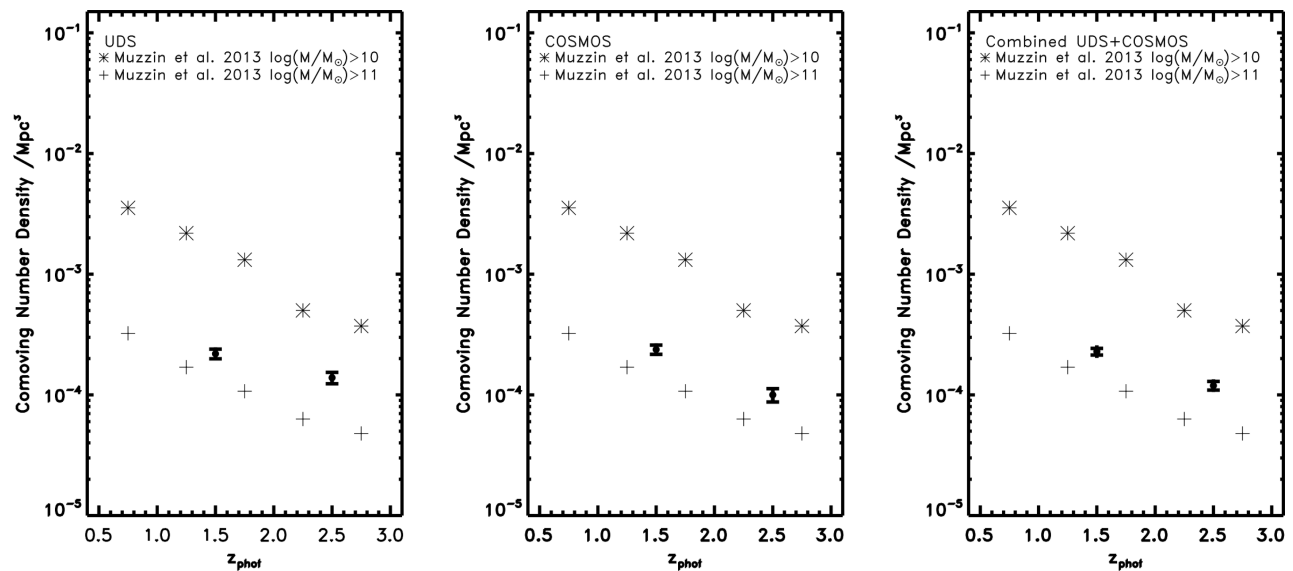


**Figure 1.** Comoving number densities of massive galaxies ($M_* > 10^{11}\,{\rm M}_\odot$) in the CANDELS–UDS (left), CANDELS–COSMOS (middle) and combined fields (right). These number densities have been over-plotted with the values from Muzzin et al. (2013) for their $M_* > 1 \times 10^{10}\,{\rm M}_\odot$ and $M_* > 1 \times 10^{11}\,{\rm M}_\odot$ mass bins, given by asterisks and crosses, respectively. As discussed, the slightly lower values reported by Muzzin et al. (2013) for galaxies within a similar mass range to this study is not unexpected given the uncertainties associated with stellar mass estimates from SED fitting, especially given the steepness of the stellar mass function in this high-mass regime.

a mass-complete sample over the redshift range of this study with a typical S/N for each object of $>50\sigma$.

The massive galaxy comoving number densities in both fields, and the combined sample, are shown in Fig. 1. These have been overplotted with the comoving number densities determined from the latest stellar mass function study at $0.2 < z < 4$ by Muzzin et al. (2013), which was conducted over the full 1.62 deg$^2$ of COSMOS covered by UltraVISTA. These plots show the comoving number densities for galaxies with derived stellar masses of $M_* > 1 \times 10^{10} \, M_\odot$ (in asterisks) and $M_* > 1 \times 10^{11} \, M_\odot$ (in crosses), illustrating how the steepness of the mass function at this high-mass end affects the number densities of objects. As can be seen, the number densities for $M_* > 1 \times 10^{11} \, M_\odot$ galaxies from Muzzin et al. (2013) are a factor of $\approx 1.6$ lower than the values for our combined sample. However, the factor of 1.6 can be accounted for by an $\sim$35 per cent decrease in the mass estimates derived by Muzzin et al. (2013) at $M_* \simeq 1 \times 10^{11} \, M_\odot$, which is consistent with the expected level of systematic uncertainty associated with stellar masses derived from SED fitting and different choices of star formation histories and stellar population age ranges.

As the sample sizes and areas in the UDS and COSMOS fields are comparable and there is good agreement between the comoving number densities of the two fields, in the following sections the science results are based on the combined UDS and COSMOS sample, except for a few cases where the results are presented individually, specifically to facilitate comparison between fields.

Finally, due to the difference in area coverage between the WFC3 pointings and the accompanying ACS parallels taken as part of CANDELS, the final sample which is subject to the multiple-component multiwavelength morphological decomposition and SED fitting comprises 178 objects which have the required photometry across all four of the CANDELS *HST* bands and have a best-fitting model with a bulge+disc.

## 2.3 Star formation rates

The star formation rates for the UDS and COSMOS samples were estimated from the best-fitting SED models and 24 μm fluxes by adopting the convention of Wuyts et al. (2011). Following this scheme, if any of the objects in the sample has a 24 μm counterpart within a 2 arcsec radius in the SpUDS and S-COSMOS catalogues, its star formation rate is given by

$$\text{SFR}_{\text{UV+IR}}[M_\odot \, \text{yr}^{-1}] = 1.09 \times 10^{-10}(L_{\text{IR}} + 3.3L_{2800})/L_\odot, \quad (1)$$

where $L_{2800} = \nu L_\nu (2800 \, \text{Å})$ and $L_{\text{IR}}$ is the contribution from radiation from hot young stars re-radiated by dust over the wavelength range 8–1000 μm. Objects which do not have 24 μm counterparts, have star formation rates calculated following Kennicutt (1998):

$$\text{SFR}_{\text{UV,dust corrected}}[M_\odot \, \text{yr}^{-1}] = 1.4 \times 10^{-28} \, L_\nu (\text{ergs} \, \text{s}^{-1} \, \text{Hz}^{-1}). \quad (2)$$

## 3 MULTIPLE-COMPONENT MORPHOLOGY FITTING

The morphologies of the 396 objects in the combined UDS and COSMOS sample have been fitted with both single and multiple-Sérsic light profiles using GALFIT (Peng et al. 2010a). The explicit procedures adopted for this analysis have been presented in Bruce et al. (2012). The fitting is conducted on $6 \times 6$ arcsec image stamps of the objects and uses an empirical point spread function (PSF) generated from a median stack of the brightest (unsaturated) stars in the individual fields. A comparison with fits determined from adopting

the latest CANDELS PSFs of van der Wel et al. (2012), which are generated from Tiny Tim models at small radii and empirical stacks further out, reveals that all fitted parameters are consistent to within a few per cent. The procedure also adopts an object-by-object background determination by calculating the median value within an annular aperture centred on each source with an inner radius of 3 arcsec and an outer radius of 5 arcsec. The multiple-component Sérsic modelling was done by fitting a set of nested models to each object comprising six models which are various combinations of $n = 1$ exponential discs, $n = 4$ de Vaucouleurs bulges and a centrally concentrated light profile component (here a PSF) to account for any nuclear starbursts or AGN. The best-fitting model is then determined by examining the $\chi^2$ statistics of each fit, where the simplest model is adopted unless a more complex model is statistically motivated at the $>3\sigma$ level. This likelihood ratio approach is adopted given the nested nature of our models, where the general case is the bulge+disc+PSF model, and penalizes the more complex fits appropriately.

This analysis provided acceptable multiple component model fits for 163 objects in the COSMOS sample, and is combined with the further 184 objects with acceptable model fits in the UDS field.

## 3.1 Mock galaxy simulations

In order to better quantify the systematic and random uncertainties in the above decomposition procedure, we have generated a grid of 9216 mock galaxies of known morphological parameters and have attempted to recover them with our fitting procedure. Similar simulations have been used previously to determine the uncertainties on fitted model parameters with GALFIT for both single-component (Häussler et al. 2007; Newman et al. 2012; van der Wel et al. 2012) and multiple-component (Davari et al. 2014) models. However, these have previously been limited to cases where the *fitted* morphologies use only a single-Sérsic model, with the exception of Lang et al. (2014) who conduct similar bulge–disc decompositions on mass maps, but in contrast to our fitting method they allow the centroid positions of their bulge and disc components to vary slightly and they explicitly limit their fits so that the disc component effective radius is always equal to or larger than that of the bulge component. Thus, for this work, we conduct our own mock galaxy simulations for $n = 4 + n = 1$ models.

All mock galaxies were generated to have the same total brightness, corresponding to the median magnitude of our combined CANDELS UDS and COSMOS sample at 21.8 mag [AB], and were constructed to have $B/T$ ratios 0.99, 0.95, 0.9, 0.75, 0.5, 0.25, 0.1, 0.05 and 0.01 to fully explore how our fitting method treats these different contributions. The models were also created with: bulge and disc effective radii of 1, 5, 10 and 20 pixels; axial ratios of 0.1, 0.3, 0.6 and 1.0; and relative position angles between the components of 0, 30, 60 and 90 degrees.

The analysis of these simulated galaxies demonstrates that in $\sim$80 per cent of cases we are able to recover $B/T$ ratios to within 10 per cent and that there is no significant systematic offset in the recovered $B/T$ ratios. Our tests also show that the sizes of the individual components can be measured to within the accuracies summarized in Table 1, for both pure bulge and disc, and mixed component systems.

For the pure bulge and disc systems, the fractional systematic offset in the measured bulge and disc sizes, respectively, ranges from 1–5 per cent, increasing with the increasing model component size, with the offset resulting in an underestimate of all sizes (except for the smallest 1 pixel model, where the sizes are consistently overestimated by $\sim$1–2 per cent). Systems which are a mixed

**Table 1.** Tabulated results for the systematic and random fractional uncertainty on the recovered sizes of the bulge and disc components from our multiple-Sérsic mock galaxy simulations. This table is split into model components of different sizes to fully illustrate how reliable the results from our fitting procedure are for different cases.

| Fractional contribution | Component | Error | 1 pixel | Model component $R_e$ 5 pixels | 10 pixels | 20 pixels |
|---|---|---|---|---|---|---|
| $B/T > 0.9$ | Bulge | Systematic offset | 1.6 per cent | 0.3 per cent | 1.6 per cent | 4.8 per cent |
| | | Random uncertainty | 4.6 per cent | 3.5 per cent | 5.2 per cent | 6.6 per cent |
| $B/T < 0.1$ | Disc | Systematic offset | 0.9 per cent | 0.9 per cent | 2.0 per cent | 3.8 per cent |
| | | Random uncertainty | 1.6 per cent | 1.6 per cent | 2.1 per cent | 3.9 per cent |
| $0.1 < B/T < 0.9$ | Bulge | Systematic offset | 1.4 per cent | 2.7 per cent | 5.8 per cent | 8.3 per cent |
| | | Random uncertainty | 12.6 per cent | 17.6 per cent | 19.1 per cent | 17.2 per cent |
| | Disc | Systematic offset | 1.8 per cent | 0.5 per cent | 2.4 per cent | 3.9 per cent |
| | | Random uncertainty | 4.2 per cent | 4.1 per cent | 6.3 per cent | 8.9 per cent |

bulge+disc systems with $0.1 < B/T < 0.9$ have similar systematic offsets in the measured disc sizes, between $1-5$ per cent, but the recovered bulge sizes of these systems are offset by $1-10$ per cent, again increasing with the increasing modelled sizes. The fractional random uncertainties on the bulge and disc size measurements, however, are roughly constant in the range $\sim 5-10$ per cent for the pure bulges and discs, and the disc components of mixed systems. There is potential evidence that the disc sizes of pure discs can be recovered more accurately; however, it is unclear whether this is significant. Again, the derived bulge sizes of the mixed systems carry a larger uncertainty of 10–20 per cent, which further demonstrates that the bulge components of mixed systems appear to be the hardest to accurately constrain (as is generally acknowledged), both in terms of their contribution to the overall light and their effective radii. Given that the uncertainties on the bulge component measurements become larger for the more extended bulge models, this effect can be understood by considering that, in order to constrain the model parameters of an $n = 4$ bulge component, any model fitting is more heavily influenced by flux at larger radii, where S/N is poorer, compared to an $n = 1$ disc-model fit which can be constrained more accurately from the central flux from the object alone.

Throughout the rest of this paper, it should be kept in mind that all $B/T$ light fractions can be considered accurate to within $\sim 10$ per cent and quoted component sizes are robust to the level of $\sim 10-20$ per cent, including any effects from systematic offsets. However, it should be noted that the accuracy with which we have been able to determine these fitted parameters results from a sample which has been selected to have S/N $\geq 50$.

In addition to the uncertainties on our fitted sizes and light fractions, the mock galaxy simulations have also allowed us to explore any degeneracies involved in fitting multiple-component models which contain a PSF component. The adoption of the additional PSF component was motivated by the high ($n > 10$) single-Sérsic fits which were obtained in Bruce et al. (2012) and the effects of including a PSF component in the single-Sérsic fits are discussed in Bruce et al. (2014). Here, we limit our discussion to the more relevant cases of the multiple-Sérsic + PSF fits.

We find that in only $\sim 3$ per cent of cases the best-fitting multiple-Sérsic model will adopt a PSF component despite the fact that no component was included in the model galaxy, although this fraction drops to $\sim 0.3$ per cent when we exclude those cases where one of the components was modelled by a single pixel effective radius. However, by explicitly examining these cases where one of the model components has an effective radius equal to one pixel, we find that in fact 90 per cent of these $r_{\rm eff} = 1$ pixel bulge models correctly avoid a best-fitting PSF component and 95 per cent of 1 pixel discs do the same.

Further exploration seems to suggest that the adoption of the PSF component for these small component cases does not appear to correlate with the flux or relative position angle of the small component, but in the case of small bulges may, understandably, be more prevalent for models with lower axial ratios, i.e. flatter, small bulge models. Moreover, for these 1 pixel component models which adopt a PSF best fit the flux of the small component is not attributed to the PSF (even within $\sim 10$ per cent) in $>70$ per cent of these cases. Instead, the majority of the flux of the small component is attributed to one or more of the bulge/disc components.

From these tests it is clear that the 'spurious' adoption of a PSF component, despite being rare, is most common in cases where there is a single pixel component, but it is not purely confined to these cases. Thus, it appears that there are some degeneracies in our fitting procedure when GALFIT is allowed to adopt an additional PSF component which are not easily quantified, although these occurrences are limited.

### 3.2 Extension to additional bands

In addition to the morphological analysis conducted on the $H_{160}$-band imaging, we have also utilized the accompanying WFC3 $J_{125}$ pointings and ACS $i_{814}$ and $v_{606}$ parallels taken in both the CANDELS UDS and COSMOS fields in order to extend our decomposition across a broad wavelength range and explore how the component contributions vary in the different bands. As the aim of this study is to explore the morphology of the majority of the assembled stellar mass within our $1 < z < 3$ galaxy sample, we have adopted the $H_{160}$-band models as they sample the galaxy light longwards of the 4000 Å break and are therefore less affected by contributions from young stars. We then fixed all model parameters at the values determined for the $H_{160}$-band fits and in the fitting procedure allowed only the magnitude of each component to vary as a free parameter. This required keeping the centroids of the objects fixed, along with the effective radius, axial ratio and position angle. During the fitting across the additional $J_{125}$, $i_{814}$ and $v_{606}$ bands, the background for each object was calculated using the same procedure developed for the $H_{160}$ contribution, by taking the median value within an annulus between 3 and 5 arcsec in radius. The $\sigma$ maps for the $\chi^2$-fitting and PSFs used were also taken from the corresponding mosaics of the individual bands, while a single bad-pixel map was applied. This map was constructed from the segmentation map of the $H_{160}$ image, rather than from each of the individual mosaics, as this was deemed to be the best way to ensure consistent masking of companions in relation to the master model fits across all bands. By fixing the rest of the model parameters, we were able to scale the contributions of the separate bulge and disc (and PSF) components across all four of the bands and provide magnitudes for these components. During

this fitting, $\sim$10–15 per cent of the sample were best fitted with a very faint second component or with a single-component fit only. In order to fully explore the best-fitting models for those objects, we constructed a grid of different component magnitudes ranging from 20 to 35 (well below the $5\sigma$ depths of the four bands) AB magnitudes (in steps of 0.1 mag). Where the fitted magnitude of a component in one of the three accompanying bands fell below the $1\sigma$ detection limit of the corresponding band, we disregarded the model fitted to that component and set it as a non-detection in the subsequent SED fitting.

As a check of the validity of this approach of fixing the model parameters to the $H_{160}$-band fit and allowing only the magnitudes of the individual component to vary across the multiwavelength fitting, we have conducted several tests of the effects of also allowing both the effective radius and the effective radius plus the axial ratio to float as free parameters. The full details for these tests are presented in Appendix . In summary, despite the naive expectation that in bluer bands the disc component of a galaxy will become more prominent and affect the goodness of a fit locked at the $H_{160}$ parameters, the additional degrees of freedom introduced by allowing the $r_e$ and $b/a$ parameters to be freely fitted significantly improve the fits for only a small sub-set of the galaxies in our sample. Moreover, for objects which were best fitted with an $H_{160}$ bulge-only model, we also experimented with allowing the addition of a disc component at the bluer wavebands but again found that this did not deliver significant improvements in the model fits, although the number of these cases was limited.

Thus, we have chosen to adopt fixed $r_e$ and $b/a$ parameter models for this multiwavelength morphological analysis in order to avoid additional degrees of freedom, which are not required and may introduce an additional degree of bias. It should also be noted that the adoption of the fixed morphological parameter approach delivered magnitudes for each component over the four-band wavelength range available in this study, which transpire to yield realistic colours for the bulges and discs. This feature of our fits verifies the validity of this approach and further demonstrates the power in applying this simplified and well-constrained procedure. A representative example fit across all four bands is shown in Fig. 2 for an object with an $H_{160}$-band best-fitting model with $B/T < 0.5$ to demonstrate how the contribution from the bulge component decreases at bluer wavelengths, while the disc-component remains more prominent in the blue bands, but is well fitted by the fixed-parameter model. Further examples of the multiband fitting of objects with best-fitting $H_{160}$-band single- and multiple-component models are also given in Appendix A.

# 4 DOUBLE-COMPONENT SED FITTING

The photometry generated from the above multiwavelength morphology fitting was then used to conduct separate bulge and disc SED fitting in order to provide more accurate masses for the two components. For this analysis, we used only the 178 objects in the combined UDS and COSMOS sample which require both bulge and disc components. As detailed in Bruce et al. (2012), one of the conditions of the morphological decomposition is the criteria that each component in an acceptable model fit must contain $\geq$10 per cent of the total flux of the object. This safeguards against selecting models which have a spurious additional component. However, for the purposes of individual-component SED fitting, those objects from the original fits which chose to incorporate a ($\geq$10 per cent) PSF component in their best-fitting model were modelled with only

a bulge and disc component to provide photometry as although the addition of a PSF component can significantly influence the fitted parameters of a single-Sérsic model fit, in the majority of cases the bulge and disc only model still provides a statistically acceptable fit.

This decision to remove the PSF component was taken as several tests into the correlation between the presence and strength of a PSF component with X-ray, 24 $\mu$m and radio counterparts have provided no clear evidence that the adoption of a PSF component is motivated by the presence of either an AGN or a nuclear starburst. Moreover, as discussed in Section 3.1, from our mock galaxy simulations, we find that there are a small number of cases ($\sim$3 per cent), where the best-fitting multiple-Sérsic model will adopt a PSF component despite the fact that no component was included in the model galaxy. Therefore, despite this low level of degeneracy, it is not clear how any such fitted PSF component, or in fact any genuine PSF component, should be correctly physically modelled in an SED fit.

It is well known that the physical properties, most importantly the stellar masses, fitted by the template-fitting SED approach can be strongly influenced by how well constrained the SEDs are by data across a broad wavelength range, particularly at the red end, where *Spitzer* IRAC data are important. In light of this, and given the limitations of using only the four-band $H_{160}$, $J_{125}$, $i_{814}$ and $v_{606}$ decomposed photometry available from our CANDELS analysis, we have adapted the SED-fitting code of Cirasuolo et al. (2007) to additionally constrain the model fits to the four-band decomposed photometry at the extreme blue and red ends. This is done by fitting the sum of the bulge and disc photometry to the single-band photometry available at $\lambda < 0.6$ $\mu$m and $\lambda > 1.6$ $\mu$m which was used previously in the full single-component SED fitting.

In brief, the SED-fitting code of Cirasuolo et al. (2007) generates a grid of different SED models from the input stellar population synthesis templates, dust correction steps, allowed ages, redshifts and star formation histories. At each point in this grid a $\chi^2$ fit is performed between the data and the SED model using the uncertainty on each photometric data point. In order to allow the additional constraints to be applied at the red and blue ends, we have adapted the SED-fitting code to allow simultaneous fitting to both the bulge and disc component photometry. This allows us to ensure that during the fitting procedure the separate bulge and disc SED models are not only fitted to the relevant decomposed photometry, but that the sum of these two models is also fitted to the overall photometry for the whole object in the $u'$ (and $B$ band for UDS), $K/K_s$, 3.6 $\mu$m and 4.5 $\mu$m bands.

The errors on the input decomposed photometry data points were determined for each component by constructing a grid of different component magnitudes ranging from $-10$ to $+10$ mag (in steps of 0.1 mag) from the component magnitude in the best-fitting $H_{160}$ model (fixing all parameters) and re-running GALFIT to generate $\chi^2$ values for each of these different magnitude grid steps. This allowed the error on, for example, the bulge component magnitude to be estimated including also the (correlated) uncertainty on the disc component magnitude by exploring the two-dimensional parameter space. The error on each component magnitude was then taken to be the $1\sigma$ level of the bulge–disc $\chi^2$-contour for each object, unless this value fell below the minimum error limit imposed from the error associated with the direct measurement of the object magnitudes from the image, where this value is taken to be 0.1 mag, in which case this 0.1 mag error was adopted.

Upon conducting tests of this approach and comparing the final SED fits of the separate and combined bulge and disc components
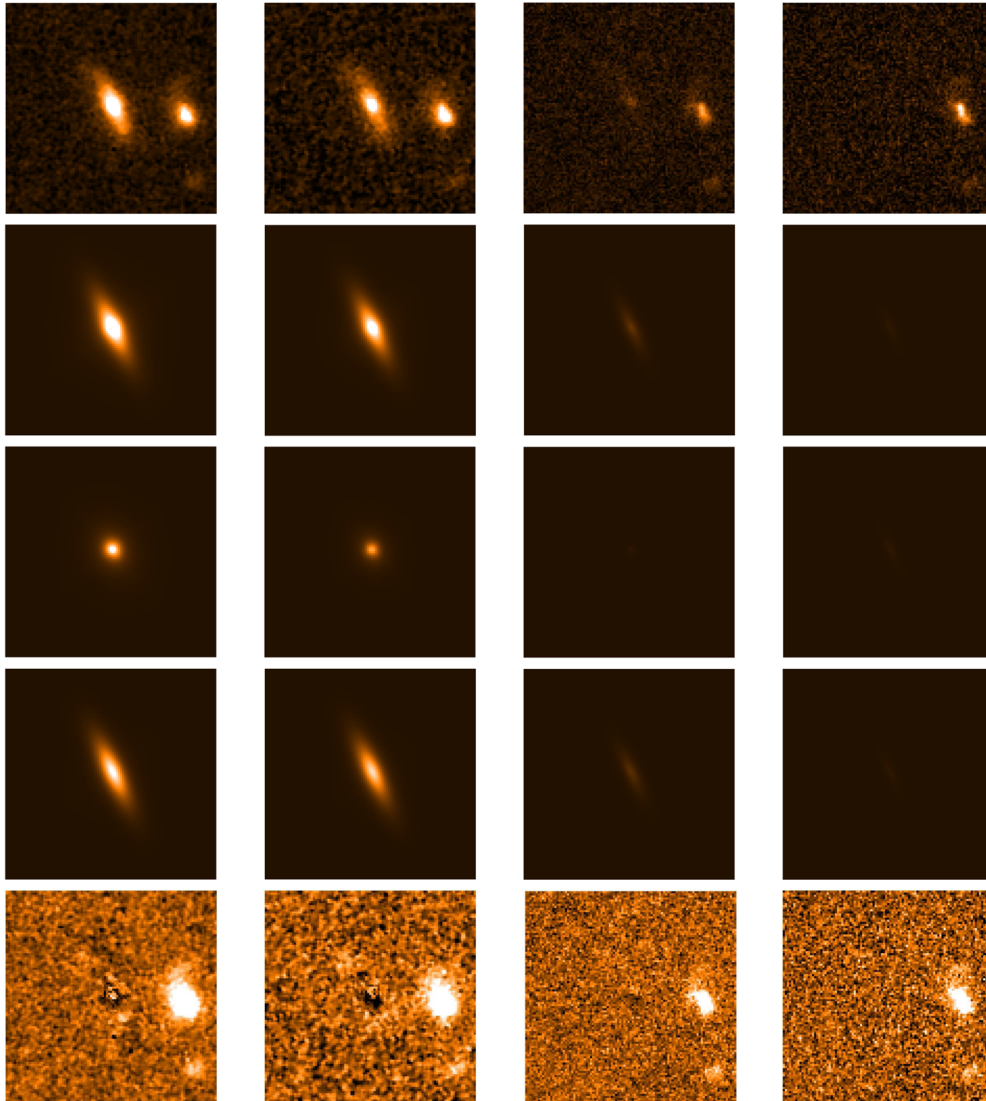
**Figure 2.** Image stamps for an example fit for a bulge+disc object with $B/T < 0.5$. Here, the stamps are again ranked from left to right by decreasing wavelength: $H_{160}$, $J_{125}$, $i_{814}$ and $v_{606}$. The vertical placement is as follows, from top to bottom: images, best-fitting combined bulge+disc models, individual best-fitting bulge components, individual best-fitting disc components, combined model residuals. The residual maps have been rescaled with respect to the image and model stamps to allow easier viewing. They have been cut at $-5$ to $+10\sigma$ of the background in the $H$ band.

to the single-component original SED fit it was discovered that in the $u'$ and $B$ bands often the flux of the total object measured from the SEXTRACTOR isomagnitude was significantly brighter than the sum of the modelled bulge and disc components. This is due to the effect of close companions in the $H_{160}$-band image which, in that band, contribute a negligible amount to the total flux of the object and have not been de-blended by SEXTRACTOR. However, as the $H_{160}$ SEXTRACTOR segmentation map has been used in dual mode to measure the isomagnitude fluxes of each of the objects in the accompanying bands, the flux of these close companions can begin to dominate the total flux at the shorter wavelengths (where the high-redshift galaxy is faint).

We have accounted for this effect by re-measuring the flux for our objects in the blue bands within a 2.5 arcsec radius aperture, which is sufficient to include the full extent of the flux from the object, whilst minimizing the contamination from the close companions.

It is these values which are used to constrain the SED fits in the $u'$ and $B$ bands.

An example SED fit is given in Fig. 3 for the same object shown in Fig. 2 with an $H_{160}$-band $B/T < 0.5$ best-fitting model. Here the single-component photometry points and best-fitting SED are given in black (points and line, respectively), and have been overplotted with the disc component photometry and the corresponding best-fitting decomposed disc SED model in blue, and the best-fitting bulge component photometry and decomposed bulge SED model in red. The sum of the best-fitting bulge and disc SED models is shown in green, and can be directly compared to the single-component fit in black. Finally, the green points, and their error bars, are the re-measured 2.5 arcsec radius photometry for the blue bands. as this object is in the UDS field it has re-measured photometry for both the $u'$ and $B$ bands. Further examples of double-component SED fits are given in Appendix B.
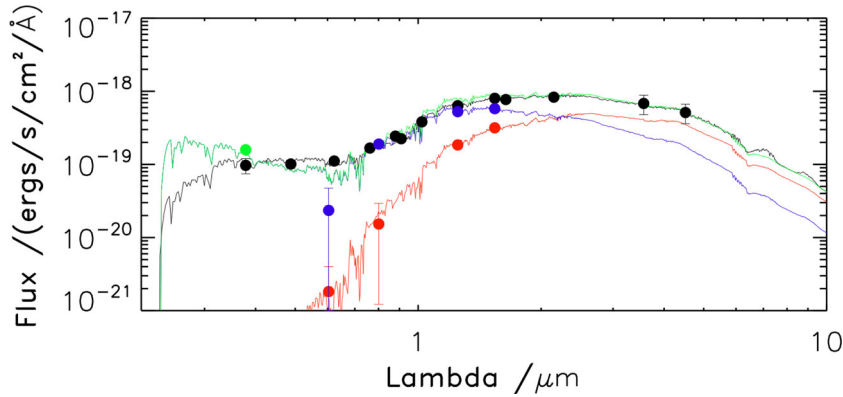
**Figure 3.** The SED fit for the example object shown in Fig. 2. Plotted as black data points and the solid black line is the total, overall galaxy photometry (with its associated error bars) and the corresponding best-fitting single-component SED. In blue is the modelled disc component photometry and the corresponding best-fitting decomposed disc SED model, and in red is the modelled bulge photometry and the best-fitting decomposed bulge SED model. Overplotted in green is the sum of the best-fitting bulge and disc SED models, which can be directly compared to the single-component fit in black and can be seen to be in good agreement with the overall galaxy photometry. Finally, the green point, and its error bar, is the re-measured 2.5 arcsec radius photometry for the $u'$ band.

## 4.1 The effect of stellar template choice on stellar mass estimates and ages

During the simultaneous SED fitting of the separate bulge and disc components, the dust attenuation, ages and star formation histories of each component were allowed to vary freely and independently. This provides a clear distinction between our approach for multiple-component SED fitting, based purely on morphological decompositions, and the 'double-burst model' fits of e.g. Michałowski et al. (2012), who fit one set of photometry points with a composite of constrained old and young stellar components.

The adoption of multiple stellar population components can significantly influence the best-fitting SED models so we have examined the impact of adopting different constraints and limitations on the input model parameters during our multiple-component fitting. For the single-component SED fitting, a minimum age limit of 50 Myr was necessary to ensure that, when fitting old objects with some on-going star formation, the $\chi^2$ minimization model parameter space did not become restricted to un-physically young ages with large amounts of dust extinction. By adding the extra degrees of freedom to the models associated with the second component, no

such age restriction was needed for the multiple-component fitting. We have also experimented with limiting the star formation histories implemented in the models which are fitted (always adopting BC03 models). By running fits with both components limited to (i) pure burst histories ($\tau = 0$), (ii) the components limited to $0.3 \leq \tau$ (Gyr) $\leq 5$, (iii) the full set of models ($0 \leq \tau$ (Gyr) $\leq 5$), we have explored the effect on the mass determinations and the accompanying fitted ages of each component.

Having conducted this comparison, we find that the full $0 \leq \tau$ (Gyr) $\leq 5$ set of star formation history models produce total bulge+disc component masses which are most comparable to the single-component SED fit masses (central panel of Fig. 4). Reassuringly, these models also represent the scenario in which we have applied the least constraints to the physical models fitted. By including the additional degrees of freedom from the second component there is no longer any physically motivated reason to restrict either component in age or star formation history, as a second younger burst, or exponentially decaying star-forming population can reasonably account for any continued or recent star formation superimposed on an older, redder population. A complete discussion of the ages
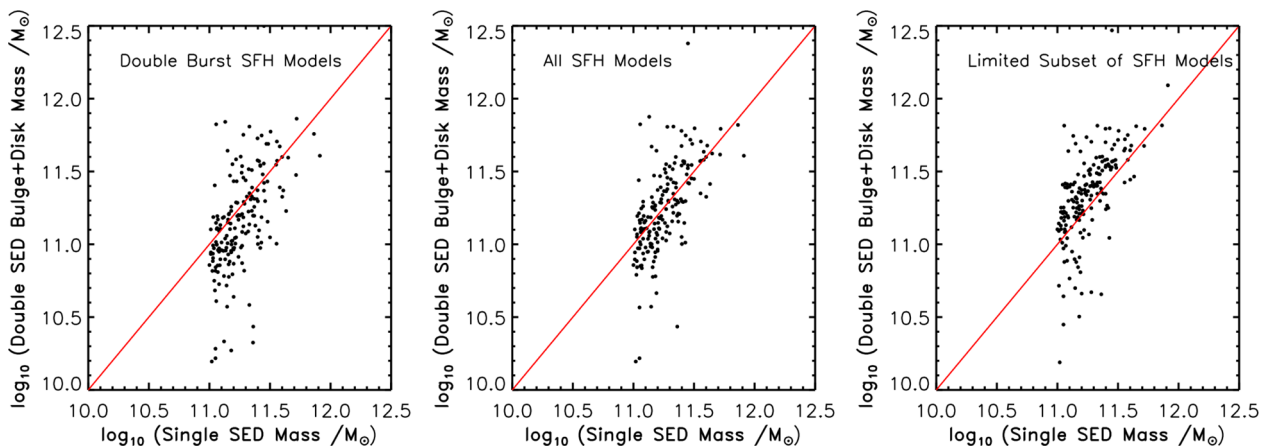


**Figure 4.** Stellar mass estimates from double-burst models (left), double $0 \leq \tau$(Gyr) $\leq 5$ models (middle) and double $0.3 \leq \tau$(Gyr) $\leq 5$ models plotted against the mass estimates from the single-component SED fits. These panels clearly demonstrate that the double $0 \leq \tau$(Gyr) $\leq 5$ models provide stellar mass estimates which are more comparable to the single-component masses.

and star formation histories of the best-fitting models is given in Appendix C.

The ability of the multiwavelength photometry for the bulge and disc components (which has been decomposed based purely on their $H_{160}$-band morphologies) to produce colours which are well fitted by physically motivated SED templates demonstrates the validity of this technique, as it is clear that no fixed correlation or pre-determined trends with colour (such as the polynomial wavelength dependences implemented in the single-Sérsic and multiple-component multiwavelength-fitting package of MegaMorph Häußler et al. (2013) and Vika et al. (2013) to fit lower S/N objects) are required.
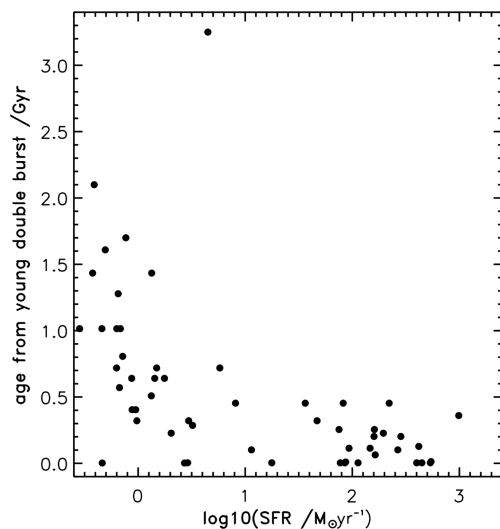
## 4.2 Separate-component star formation rates

In addition to the overall galaxy specific star formation rate (sSFR) estimates discussed in Section 2.3, the decomposed sSFRs of the individual components have also been determined from SED fitting of the individual-component photometry using models which include bursts and exponentially declining star formation histories in the range $0.1 \leq \tau\,(\mathrm{Gyr}) \leq 5$. Previous single-component SED-fitting studies by Wuyts et al. (2011) found, when comparing star formation rates determined from dust-corrected SED fitting with those from combinations of non-dust-corrected UV and infra-red contributions (SFR$_{\mathrm{UV+IR}}$) that the adoption of very sharply declining star formation $e$-folding time-scales, $\tau < 0.3$ Gyr, provided statistically improved SED fits, but that these fits had stellar population ages which were unrealistically young and had star formation rates that were systematically lower than the estimates derived from SFR$_{\mathrm{UV+IR}}$. As a result, they suggested removing such short $e$-folding time-scales for SED fitting and it is this approach which we have adopted for the SED fitting of the single components.

However, from the careful SED fitting comparisons conducted for the double-component models, we have found that the extra degrees of freedom incorporated with the addition of the second component remove the bias of including these sharply declining star formation histories in the SED fits. This has been found from examination of the ages of the old stellar component, which show that they are no longer biased towards implausibly young values and show an age distribution comparable to the ages of the single-component fits which were limited to the $0.3 \leq \tau\,(\mathrm{Gyr}) \leq 5$ subset (see Appendix C Fig. C1). Furthermore, by adding a second component, we have also allowed the model fits to include the case of burst star formation histories. The inclusion of a second component allows for the superposition of an old population, which experienced a burst of star formation in the past, with an additional population exhibiting on-going or slowly declining star formation. However, while the incorporation of burst models in the double-component SED fitting has been validated by the above exploration, burst models obviously do not provide any estimates for even low levels of on-going star formation in young components.

As a result, the star formation rates derived for the separate-component modelling may be underestimated in comparison with the star formation rates derived from the single-component SED fitting, which was forced to have some level of on-going star formation activity by adopting $0.3 \leq \tau\,(\mathrm{Gyr}) \leq 5$. Thus, in order to better reconcile these two approaches, for the double-component model results we adopt different sSFR estimates for the several possible modelled scenarios, as follows.

(i) For fits with double-$\tau$ ($0.1 \leq \tau\,(\mathrm{Gyr}) \leq 5$) models, we use the UV dust-corrected star formation rates (using the independent



**Figure 5.** Relation between the ages of the young component of the double-burst models and the star formation rates from the single-component SED fit, illustrating good overall agreement between the ages of the components to which all star formation activity in the galaxy has been attributed, and the overall star formation rates for the galaxies.

component best-fitting $A_v$ extinction values) from the SED models of each component and divide through by the corresponding modelled mass of those components to provide the sSFR for each component separately.

(ii) For fits with double-burst models, where both components are older than 500 Myr, we deem them both to be passive and allocate them a sSFR $= 10^{-12}$ yr$^{-1}$. Where one burst component is young ($<500$ Myr), we attribute the entire star formation rate derived from the limited single-component SED fitting to that young component and calculate the sSFR by dividing through by the mass of that component modelled from the decomposed photometry, and assume the old component is passive and adopt a sSFR $= 10^{-12}$ yr$^{-1}$.

(iii) For a single burst $+ \tau$ model, we generate a sSFR for the $\tau$ model based on the UV dust-corrected SED fitting star formation rate and mass of that component from the decomposed photometry and for the burst model we adopt the passive limit of sSFR $= 10^{-12}$ yr$^{-1}$.

In this way, we have best accounted for the mass decomposition of the objects, by adopting a model which can incorporate both a burst and steeply declining star formation rate for one or both of the components, and have provided an indication of the star formation rates in each component, which otherwise would not have been achievable for model fits of burst star formation histories. In fact, Fig. 5 demonstrates the general correlation between the ages of the young components from the double-burst models and the star formation rates estimated from the single-component SED fitting. Additional checks of this approach are presented in Appendix C.

## 5 MORPHOLOGICAL EVOLUTION

The evolution of the overall morphology of galaxies at $1 < z < 3$ can provide important insights into the physical processes which govern galaxy evolution, especially as there is growing evidence that it is within this epoch that massive galaxies are undergoing dramatic structural transformations (e.g. Buitrago et al. 2008; Förster Schreiber et al. 2009; Mortlock et al. 2013). For completeness, we first present the separate CANDELS-UDS and COSMOS samples

**Table 2.** Top : the percentages of the re-selected UDS sample of 184 objects with multiple-component best fits corresponding to each of the six fitted models. Middle: the percentages of the final COSMOS sample of 163 objects for each best-fitting model. Bottom: the percentages of the combined UDS+COSMOS samples of 347 objects for each of the best-fitting models.

|  | Bulge | Bulge +PSF | Disc | Disc +PSF | Bulge +disc | Bulge+disc +PSF |
|---|---|---|---|---|---|---|
| UDS | $10 \pm 2$ per cent | $1 \pm 1$ per cent | $17 \pm 3$ per cent | $8 \pm 2$ per cent | $59 \pm 7$ per cent | $5 \pm 2$ per cent |
| COSMOS | $15 \pm 3$ per cent | $2 \pm 1$ per cent | $15 \pm 3$ per cent | $13 \pm 3$ per cent | $42 \pm 6$ per cent | $13 \pm 3$ per cent |
| Combined | $12 \pm 2$ per cent | $2 \pm 1$ per cent | $16 \pm 2$ per cent | $10 \pm 2$ per cent | $51 \pm 5$ per cent | $9 \pm 2$ per cent |

split by fractions into the different best-fitting models, to allow comparison between the fields.

From Table 2, it can be seen that, overall, there is good agreement between the fractions of objects best fitted by the different models between the CANDELS-UDS and COSMOS samples. However, this direct comparison also highlights that there are fewer objects fitted with a bulge+disc model in COSMOS compared to UDS, but more have a bulge+disc+PSF best-fitting model. Nevertheless, this difference is small, and while only part of the discrepancy can be attributed to cosmic variance (Newman & Davis 2002), the small number statistics involved do not provide significant evidence for any biases in the fitting of morphologies between these two fields. Moreover, it should also be noted, from this table, that overall the fractions of 'pure' bulge and disc galaxies are statistically comparable in both fields. The fractions for the overall combined sample are given in the bottom line of Table 2, where they can be seen to be statistically consistent with those given for both the UDS and COSMOS fields.

### 5.1 Trends with redshift

In order to explore how the overall morphologies of these massive $1 < z < 3$ galaxies evolve with redshift, and keeping in mind that our fitted $B/T$ fractions are accurate to better than $\sim$10 per cent, we have binned the samples at $z < 2$ and $z > 2$ and have calculated the comoving number densities of objects split according to the different morphology discriminators: $B/T > 0.5$ and $D/T > 0.5$ (where $D/T$ is used to avoid confusion arising from a PSF component contributing a significant fraction); $B/T > 0.7$, $D/T > 0.7$ and intermediate objects; and $B/T > 0.9$ and $D/T > 0.9$ and intermediate objects. The results from this binning, determined based on the multiple-component SED fitting masses, are shown in Fig. 6, where the three rows are split further into the UDS, COSMOS and combined samples. These number densities have been overplotted with the total number density of galaxies in each redshift bin to demonstrate how the overall number of galaxies falls above $z = 2$. Compared to comoving number density fractions obtained from using cuts based on the $H_{160}$ light fractions alone, these plots have a larger number of bulge-dominated systems, which is to be expected from the decomposed mass analysis due to the more evolved stellar populations and consequently higher mass-to-light ratios of bulge systems compared to discs. Nevertheless, to first order these plots reveal that, as previously found in Bruce et al. (2012), in the UDS field the massive galaxy population is dominated by disc structures above $z = 2$ and becomes an increasing mix of bulge+disc morphologies below this, with no evidence even by $z = 1$ for the emergence of pure bulge systems. The rise in intermediate objects is similar in both the UDS and COSMOS fields. However, the COSMOS sample appears to show a less significant trend for the demise of dominant discs below $z = 2$ as the redshift evolution for the $D/T > 0.7$ and $D/T > 0.9$ cuts is much flatter within the errors, and actually increases with redshift for the $D/T > 0.5$ cut.

These results appear to reveal significant evidence for a difference between the two fields.

However, when considering the evolution in the number of objects with disc- and bulge-dominated morphologies in these plots, the overall evolution in the total number of galaxies in each redshift bin must also be taken into account, as it can clearly be seen that the total number of $z > 2$ galaxies is significantly less than the number of objects at $z < 2$. In order to better interpret these results, we have plotted the fraction of the total number of objects in each redshift bin which are split into bulge- and disc dominated according to the three different cuts in Fig. 7, again using the decomposed stellar mass estimates. From inspection of this plot, the variation between the disc-dominated trends with redshift between the fields is somewhat less prominent, although still present, and the evolution of the intermediate bulge+disc fractions remain consistent. This is also the case if the morphological cuts were based only upon the $H_{160}$-band light fractions.

This discrepancy between the two fields is somewhat surprising given the results from Table 2, which show that there are the same fraction of galaxies classified as 'pure' bulges and discs in both fields. Further exploration of this issue revealed differences in the photometric-redshift distributions of both the bulge- and disc-dominated systems between the fields. These distributions are shown in Fig. 8 with the distributions for the UDS field on the left given in blue for the $D/T > 0/5$ galaxies and red for the $B/T > 0/5$, and the COSMOS fits on the right. It can be seen from these figures that there is a sharp peak in the redshift distribution of disc-dominated galaxies in the UDS at $z \approx 2$, which is perhaps indicative of a photometric-redshift focusing effect. There is also a steeper decline in the number of bulge-dominated systems above $z \sim 2$ in the UDS field compared to COSMOS. These two effects act together to produce a flatter redshift evolution of discs compared to bulges in the COSMOS field.

The peaked redshift distribution of the disc-dominated objects in the UDS required further exploration to ensure that our results have not been biased by photometric-redshift focusing effects. This issue is well known for objects with relatively flat SEDs where there are no strong breaks for the SED template fitting approach to fit to and so may preferentially occur for the disc-dominated galaxies in our sample. Plausibly, this may also be more of an issue for the UDS sample due to the accompanying optical and near-IR photometry utilized for the SED fitting, as the UDS field makes use of much shallower $Y$-band data compared to the COSMOS field.

In order to test for this effect, we have cross-matched our sample with the CANDELS-UDS photometric-redshift catalogue of Dahlen et al. (2013). The Dahlen et al. photometric-redshift catalogue is constructed using a Bayesian approach which uses the redshift probability distributions of six different photometric-redshift fits using different photometric-redshift fitting codes. Adopting the Dahlen et al. redshifts for our sources has a marginal effect on the redshift distribution of the disc-dominated galaxies in our UDS sample, but does not affect the trends for the combined UDS and
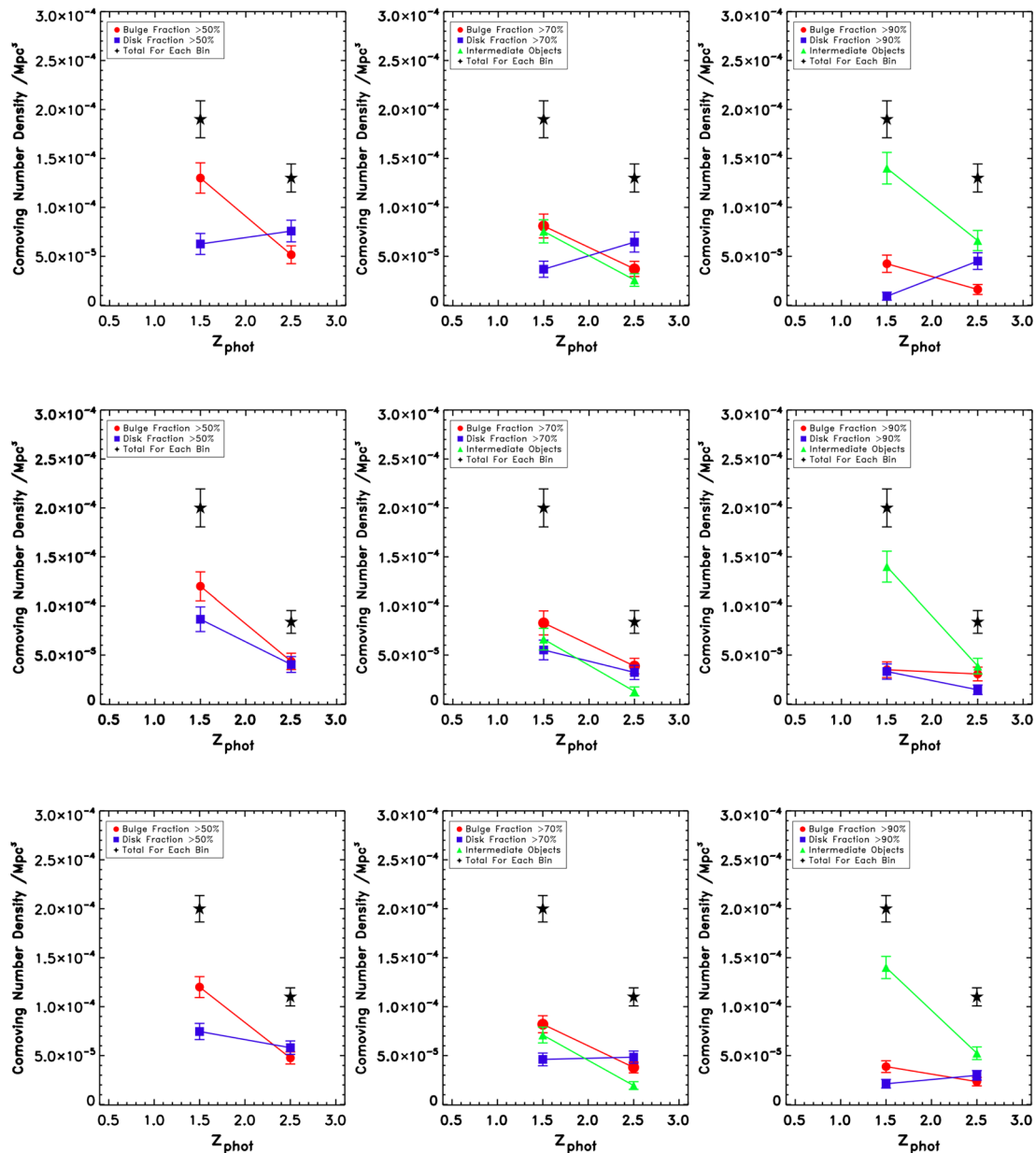
**Figure 6.** The comoving number densities of the samples split by the different bulge and disc-dominated criteria according to their SED-fitting individual-component stellar mass fractions. The top panels show the UDS sample, the middle panels are the COSMOS sample, and the bottom panels are for the combined UDS+COSMOS total sample. The blue data points and lines are for the disc-dominated galaxies, shown in red are the bulge-dominated galaxies and in green are galaxies classified as intermediate bulge+disc systems. The left-hand panels split the populations according to $B/T > 0.5$ and $D/T > 0.5$, the middle panels adopt $B/T > 0.7$, $D/T > 0.7$ and intermediate objects, and the right-hand panels use $B/T > 0.9$, $D/T > 0.9$ and intermediate objects.

COSMOS sample. Therefore, we have concluded for this work that our overall results are not biased by this issue and so present the trends displayed by the combined UDS and COSMOS samples, simply noting that the separate UDS and COSMOS samples display some differences which are at least partly due to cosmic variance (Newman & Davis 2002).

In conclusion, the combined UDS and COSMOS samples reveal that the fraction of bulge-dominated galaxies remains relatively flat across the $1 < z < 3$ redshift range covered by this study, particularly when considering the 'pure' bulges with $B/T > 0.9$, where even at $z < 2$ these most massive galaxies are predominantly mixed bulge+disc systems and a significant fraction of 'pure' bulges, comparable to the giant elliptical systems which

dominate the massive galaxy population locally, are yet to emerge. Despite the above discussion, there is still some evidence for the demise of disc-dominated systems below $z = 2$, both from the fractions determined from the $H_{160}$ light fractions and the decomposed stellar masses. This becomes particularly evident when comparing the fraction of disc-dominated galaxies to not only the bulge dominated, but also the intermediate objects, as it is clear that $z = 2$ still marks a key phase below which these most massive galaxies gain an increasing contribution from bulge components. The strongest trend evident from this analysis is the increase in the intermediate classification with decreasing redshift, which may reveal the rise of S0 type galaxies within this redshift regime. This trend is noticeably stronger when cutting by $H_{160}$ light fraction than decomposed mass.
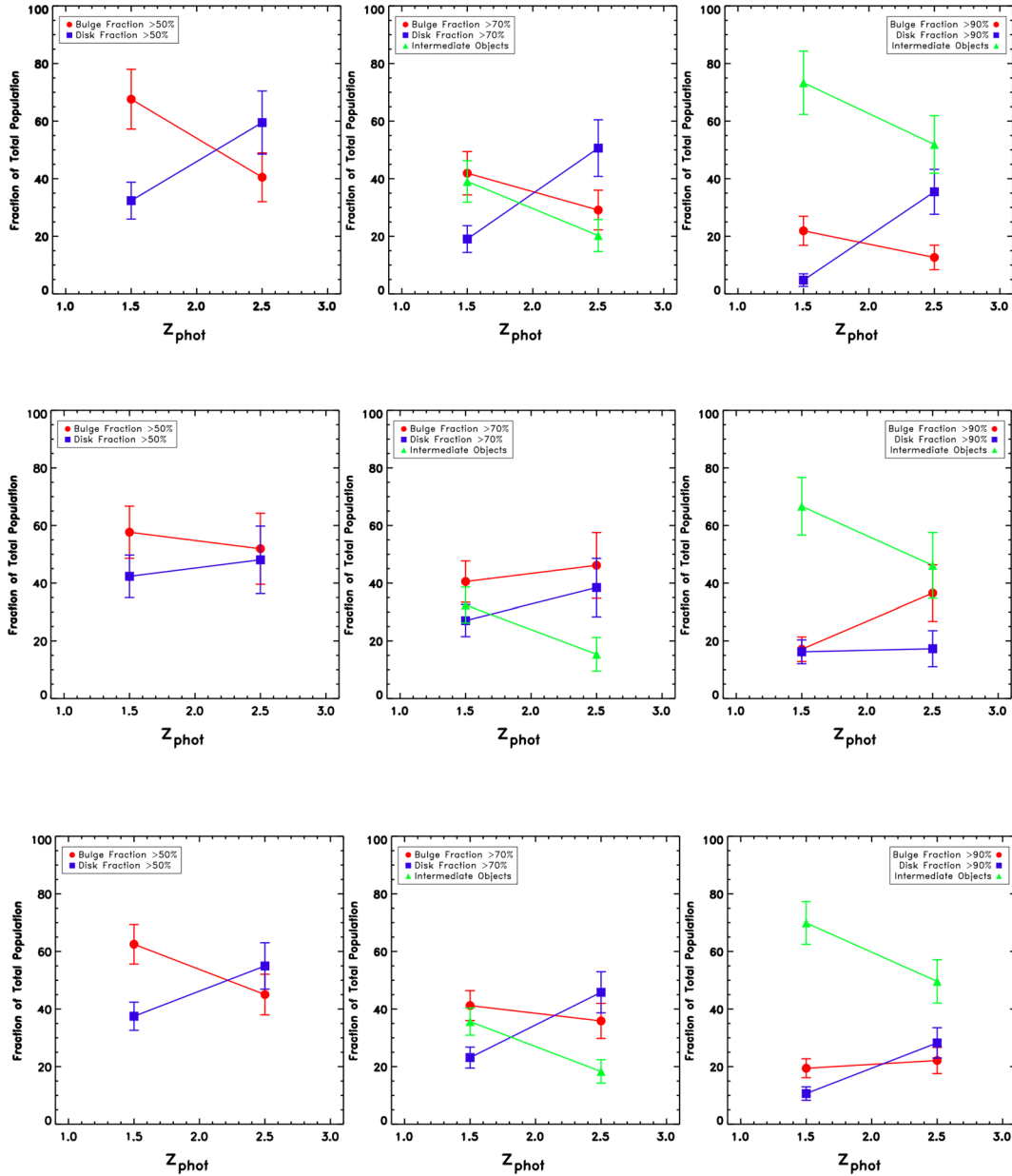
**Figure 7.** The fraction of the total number of objects in each sample classified by the different bulge and disc-dominated criteria according to their decomposed SED-fitting stellar mass fractions. The top panels show the UDS sample, the middle panels are the COSMOS sample and the bottom panels are for the combined UDS+COSMOS total sample. The same configuration is used as in Fig. 6. By adopting the fractions determined from the stellar mass contributions and comparing them to those from the $H_{160}$ light fractions, it can be seen that the most massive galaxies become increasingly mixed bulge+disc systems morphologically from $z \sim 3$ to 1, but their masses become even more bulge dominated.

However, this is to be expected from the fact that bulge components are more dominant in terms of their contribution to the mass of the galaxy, so the decomposed mass trends show a weaker trend in the increase of intermediate systems but display a larger increase in the fraction of bulge-dominated systems.

# 6  STAR FORMATION EVOLUTION

In the following sections, we combine the information from the decomposed morphological analysis with star formation activity estimates from both the overall galaxy, and the decomposed estimates for the separate bulge and disc components, to probe how the morphological transformations witnessed in this $1 < z < 3$ redshift regime are linked to the process, or processes, responsible for star formation quenching. In order to facilitate better comparison with other studies, we have also compared our passivity cut at sSFR $< 10^{-10}$ yr$^{-1}$ from the overall galaxy SED fitting to colour–colour cuts from *UVJ* diagrams following Williams et al. (2009), and find good agreement between the two techniques for separating star-forming and passive galaxies.

## 6.1  Star formation and morphology

In Figs 9–11, we present plots of the total sSFR for each galaxy against both the single Sérsic-index and the bulge/total light fraction for the UDS, COSMOS and combined fields, respectively.
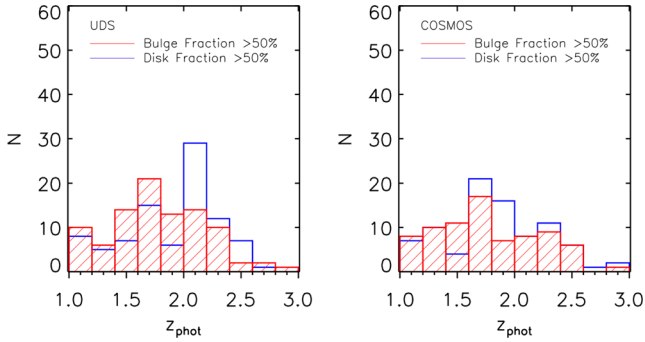
**Figure 8.** Redshift distributions of the bulge- and disc-dominated components using the $B/T > 0.5$ and $D/T > 0.5$ criteria for the UDS and COSMOS samples separately. Comparison of these distributions reveals a peak in the redshift distribution of the disc-dominated galaxies in the UDS at $z \sim 2$, possibly indicative of redshift focusing in this sample. However, this comparison also shows that the number of bulge-dominated galaxies falls-off more steeply in the UDS than in COSMOS. This abundance of $z > 2$ bulge-dominated galaxies in COSMOS will also contribute to the flatter evolution of the fraction of disc-dominated galaxies in COSMOS.
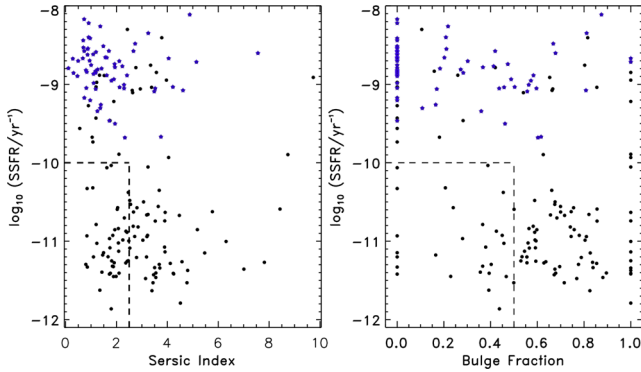


**Figure 9.** sSFR for the galaxies in the UDS sample versus Sérsic index (left) and bulge/total $H_{160}$ light fractions (right). Galaxies with a 24 µm counterpart from either SpUDS or S-COSMOS have been highlighted by the blue stars, and a box has been placed around the passive (sSFR < $10^{-10}$ yr$^{-1}$) disc-dominated galaxies as judged by both $n < 2.5$ and $B/T < 0.5$. Comparison with the similar figure in Bruce et al. (2012) shows that the adoption of the re-evaluated star formation rates for the UDS sample has removed objects which have a 24 µm counterpart from the passive region of the plot, but a significant number of passive discs and star-forming bulges remain.

The fraction of passive galaxies (from the overall galaxy sSFR) which are disc-dominated and star-forming galaxies which are bulge dominated in each field are given in Tables 3 and 4. There is also a comparable fraction of both passive disc-dominated and star-forming bulge-dominated galaxies in both fields, judging morphology by either the single-Sérsic index cut at $n = 2.5$ or by the decomposed $B/T = 0.5$ measure, with ~30 per cent of all passive or star-forming galaxies being disc- or bulge dominated, respectively.

However, one notable variation between the fields is the larger number of $B/T = 0$ passive discs in COSMOS than in the UDS. For the COSMOS field there are five objects within this range that are best fitted by a 'pure' disc, and another 10 objects which are best fit with a disc+PSF model (it is worth noting that for the disc+PSF fits none of the PSF fractions exceed 30 per cent, thus these objects would remain disc dominated even in the extreme case where all of the PSF flux was attributed to the bulge component). The corresponding numbers for the UDS are three 'pure' discs and four
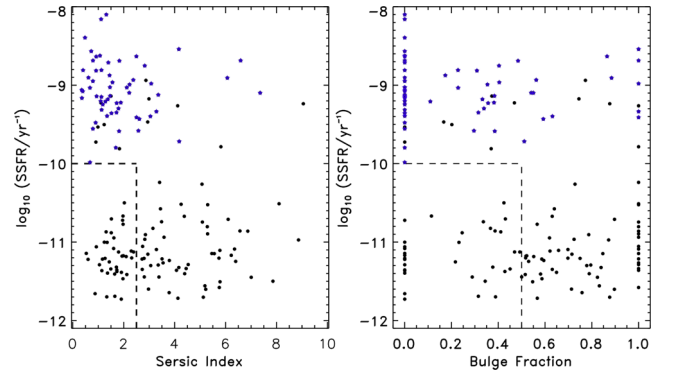


**Figure 10.** sSFR for the galaxies in the COSMOS sample versus Sérsic index (left) and bulge/total $H_{160}$ light fractions (right). Galaxies with a 24 µm counterpart from either SpUDS or S-COSMOS have been highlighted by the blue stars, and a box has been placed around the passive (sSFR < $10^{-10}$ yr$^{-1}$) disc-dominated galaxies as judged by both $n < 2.5$ and $B/T < 0.5$. In comparison to the UDS sample, the COSMOS sample has the same overall number of objects in the star-forming bulge- and disc dominated and the passive bulge- and disc-dominated sub-populations; however, they do appear to be more passive $B/T = 0$ discs in COSMOS, but these numbers are very small and may be affected by cosmic variance.
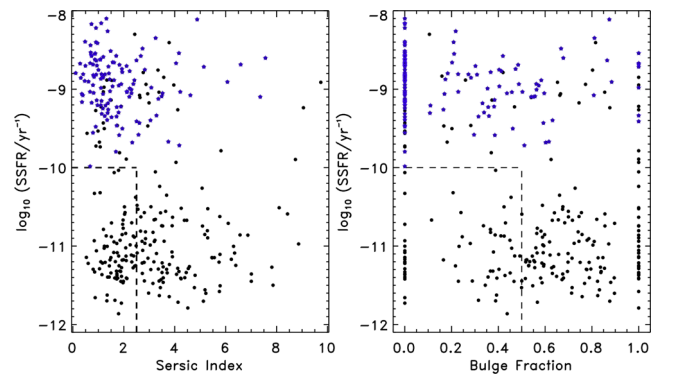


**Figure 11.** sSFR for the galaxies in the combined UDS+COSMOS sample versus Sérsic index (left) and bulge/total $H_{160}$ light fractions (right). Galaxies with a 24 µm counterpart from either SpUDS or S-COSMOS have been highlighted by the blue stars, and a box has been placed around the passive (sSFR < $10^{-10}$ yr$^{-1}$) disc-dominated galaxies as judged by both $n < 2.5$ and $B/T < 0.5$.

**Table 3.** The fractions of passive galaxies which are disc dominated, split by field and using both the single-Sérsic and multiple-component classifications.

| Field | $n < 2.5$ | $B/T < 0.5$ |
| --- | --- | --- |
| UDS | $38 \pm 7$ per cent | $30 \pm 7$ per cent |
| COSMOS | $43 \pm 8$ per cent | $37 \pm 7$ per cent |
| Combined | $41 \pm 5$ per cent | $33 \pm 5$ per cent |

**Table 4.** The fractions of star-forming galaxies which are bulge dominated, split by field and using both the single-Sérsic and multiple-component classifications.

| Field | $n > 2.5$ | $B/T > 0.5$ |
| --- | --- | --- |
| UDS | $33 \pm 8$ per cent | $31 \pm 6$ per cent |
| COSMOS | $26 \pm 7$ per cent | $26 \pm 7$ per cent |
| Combined | $30 \pm 5$ per cent | $29 \pm 5$ per cent |

disc+PSF objects. Given the low number statistics involved, and that overall, as shown in Table 2, the same fraction of the population in both samples has been best fitted by disc and disc+PSF models, it is difficult to draw firm conclusions from these numbers. Moreover, given that the addition of a PSF component may indicate the presence of an AGN or nuclear starburst, we have tried to search for any evidence of AGN activity from the X-ray and radio catalogues available in both the UDS and COSMOS fields, but found no counterparts within a 4 arcsec matching radius for the X-ray catalogues and 2 arcsec matching radius for the radio catalogues, for any of the 'pure' discs or disc+PSF fits. Given the objects being fitted are from CANDELS images of the same S/N there is also no reason to attribute this difference between fields to biases from the adoption of a spurious additional PSF in the fitting procedure, as explored with the simulations. In addition to this, from examining the spatial positioning of these objects in both fields, we find no obvious evidence of clustering. Thus, we simply conclude that the classification of these objects is equally robust and unbiased in both fields, and attribute the offset in the small numbers to shot noise.

The verification of a significant population of both star-forming bulge-dominated galaxies and passive disc-dominated objects is particularly interesting as they may suggest that the processes which quench star formation are distinct from those which drive morphological evolution. Despite previously limited evidence for these populations (McGrath et al. 2008; Stockton et al. 2008; Cameron et al. 2011; van der Wel et al. 2011; Bruce et al. 2012; Wang et al. 2012), more recently, the presence of a significant passive disc-dominated population has been corroborated by studies such as McLure et al. (2013), Chang et al. (2013b), Fan et al. (2013), Lee et al. (2013), Talia et al. (2013) and Lang et al. (2014). However, these studies use a mixture of single-Sérsic, non-parametric and visual morphological classifications, with the exception of van der Wel et al. (2011) and Lang et al. (2014) who perform double-component $n = 1$ +free fits and $n = 1 + n = 4$ fits but adopt star formation rates for the galaxy as a whole. This approach may be prone to misclassification if, for example, the bulge component of the galaxy dominates in terms of stellar mass in which case the galaxy should arguably no longer be classified as disc dominated and, moreover, the sSFR of the disc-only component may in fact be above the passivity threshold. This is clearly also a concern for the star-forming bulge-dominated galaxies, where one might expect the decomposition to reveal that, while the overall galaxy sSFR $> 10^{-10}$ yr$^{-1}$, the bulge component itself is passive and the star formation activity is limited to the disc component. In order to explore how many of the passive discs and star-forming bulges in our sample may be prone to misclassification based on the adoption of the overall galaxy star formation rate and morphological light-based bulge and disc fractions, we have examined the individual-component stellar masses and star formation rates for all objects within these populations.

## 6.2 Passive discs

Of the 184 passive galaxies in the full sample, only 146 are covered by both the ACS and WFC3 pointings and so have been modelled by the decomposed SED fitting.

Out of these 146 passive galaxies, 16 have been best fitted with either a 'pure' disc or disc+PSF model (13 in COSMOS and three in the UDS). These objects have therefore not been subjected to the decomposed SED fitting, and given the above discussion on the lack of any 24 μm, X-ray or radio counterparts for these systems, we have no reason to assume they have any obscured star formation and/or AGN activity. Thus, we have adopted the overall galaxy star

formation rate for these galaxies and report them as genuine pure passive discs. For completeness, for the case of only the 'pure' discs, there are two in the UDS and four in COSMOS.

In addition to the 'pure' disc and disc+PSF fits, there are 30 objects which are passive and disc dominated which have been fitted with a multiple-component model. In order to report the most conservative and robust fraction of passive disc-dominated galaxies in our sample using the decomposed stellar mass and star formation rate estimates, we have adopted the criteria that these objects must be classified as passive with a total bulge+disc decomposed sSFR $< 10^{-10}$ yr$^{-1}$ *and* a decomposed disc sSFR $< 10^{-10}$ yr$^{-1}$ (where we have used the decomposed disc stellar mass to calculate the sSFR). This leaves 26/30 candidates as passive, where these objects all additionally had decomposed bulge sSFR $< 10^{-10}$ yr$^{-1}$. Finally, to remain in the passive disc-dominated population, we required that the objects must be classified as disc dominated by their decomposed disc/bulge+disc stellar masses. Imposing this criterion removed 15 galaxies and left 11 galaxies which are genuinely passive and disc dominated by even our strictest definitions.
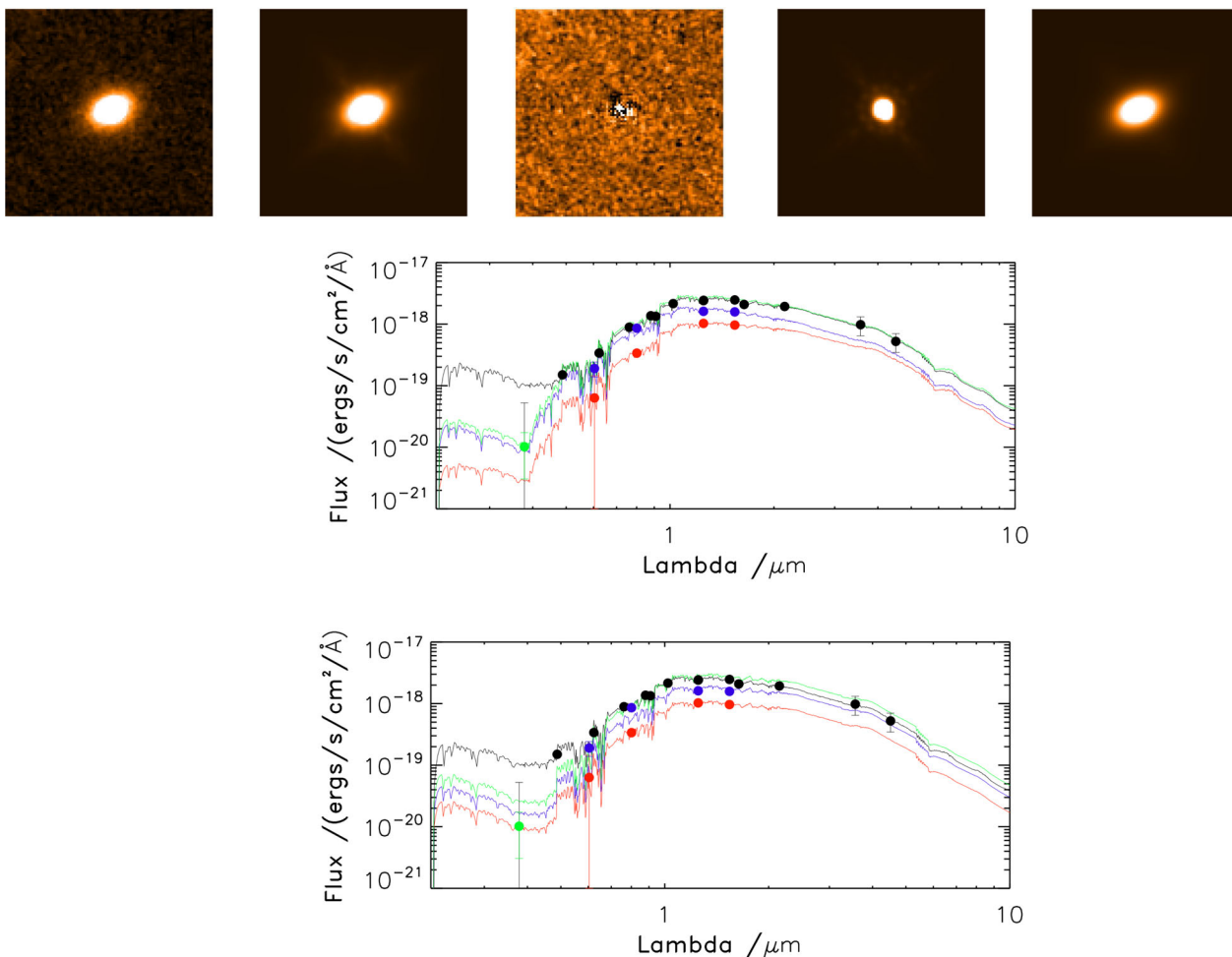
These 11 passive disc-dominated galaxies were then combined with the 16 'pure' disc and disc+PSF objects and are taken as a fraction of the 146 passive galaxies. This provides the estimate that (27/146) $18 \pm 5$ per cent of all passive galaxies are disc dominated. This fraction becomes $12 \pm 3$ per cent if the objects with a best model fit with a disc+PSF are removed. However, given that the results from our simulations reveal that in $\geq 90$ per cent of models which have a compact bulge component our fitting procedure is able to correctly attribute the flux from the model component to a bulge rather than a PSF, it is evident that these disc+PSF fits are not significantly contaminated by disc-dominated objects which host a centrally compact bulge, and in any case the PSF fractions of these fits do not exceed 30 per cent. Therefore, these objects are still disc dominated and there is no obvious reason to remove them.

An example of one of the passive disc-dominated galaxies which is best fitted with a bulge+disc model and has been subjected to decomposed SED fitting is shown in Fig 12, where we have displayed the master $H_{160}$ 6 × 6 arcsec image, the best-fitting bulge+disc model, the bulge component of the best-fitting model, the disc component of the best-fitting model, and the residual stamp. These images clearly illustrate that this is a genuinely morphologically disc-dominated galaxy, the disc component is not some remnant of poor fitting, and that the model is a good fit to the galaxy. We have also included the best-fitting model SED output for this galaxy. As before, the blue data points and line represent the disc component, the red data points and line represent the bulge component, and the sum of the best-fitting bulge and disc SED model is given in green. This SED demonstrates the quality of the fit to the photometry and the genuine passivity of the disc component. In order to provide the most conservative estimates of the passive disc-dominated fraction, we have also ensured that even by adopting the limited sub-set of SED models with $0.3 < \tau(\text{Gyr}) < 5$, which forces the galaxy to have at least some low level of measurable on-going star formation, the disc components of this population remain passive. The best-fitting SED using this limited $\tau$ model sub-set is given in the bottom panels of Fig. 12 and serves to further confirm the classification of this object.

## 6.3 Star-forming bulges

We have also examined the decomposed stellar mass and star formation rate estimates for the star-forming bulge-dominated systems. Again, only a limited sub-set of these objects have been covered

**Figure 12.** One of the genuinely passive disc-dominated galaxies as judged by the most conservative criteria on the decomposed fits. The $H_{160}$ $6 \times 6$ arcsec stamps are shown. The first row, from left to right, contains the image stamp, the best-fitting multiple-component model, the residual map, the best-fitting bulge model component only and the disc only component. The second row displays the best fit $0 < \tau(\mathrm{Gyr}) < 5$ decomposed SED models. For completeness, the bottom row contains the $0.3 < \tau(\mathrm{Gyr}) < 5$ SED fits, which force the models to adopt a minimum low level of on-going star formation.

by both WFC3 and ACS pointings, which gives a total of 136 star-forming galaxies. Out of these, 11 are best fitted by 'pure' bulges (comprising six objects in COSMOS and five objects in the UDS) and there are an additional two objects best fitted by bulge+PSF models. There are also 24 candidate star-forming bulge-dominated galaxies with best-fitting multiple component models.

For these 24 candidate star-forming bulge-dominated systems, we then insist that in order to remain in this sample they must be bulge dominated in terms of their bulge/bulge+disc decomposed stellar mass fractions, and that the bulge sSFR $> 10^{-10}\,\mathrm{yr}^{-1}$. Only four objects meet these criteria, as in the vast majority of cases the star formation rate decomposition reveals that it is the disc components which are active. For all four of these objects, the disc component has a sSFR $< 10^{-10}\,\mathrm{yr}^{-1}$. As above, we also further restrict the sample to the most conservative fraction by requiring that, when the limited $0.3 < \tau(\mathrm{Gyr}) < 5$ SED models are adopted, the bulge component remains star forming. In one of the four cases the limited $\tau$ SED models fit both the disc and bulge components with sSFR $< 10^{-10}\,\mathrm{yr}^{-1}$. This suggests that this best-fitting model is particularly degenerate so this object is removed from the sample and we have retained only three robust star-forming bulge-dominated galaxies.

Visual examination of one of these object revealed that it was a misclassified AGN and has in fact been identified as a Type1,

unobscured, AGN by Trump et al. (2009). Therefore, we have removed it from the star-forming bulge population and combine the two remaining bulge-dominated systems with the 11 'pure' bulges and the two bulge+PSF fits, and comparing them to the 136 star-forming galaxies also with ACS coverage, provides an estimate for (15/135) $11 \pm 3$ per cent of all star-forming galaxies to be bulge-dominated systems.

These two star-forming bulge-dominated bulge+disc systems are shown in Figs 13 and 14. These plots show the master $H_{160}$ and blue $v_{606}$ stamps for the images, best-fitting models, separate model bulge and disc components and residuals, and justify that for the first two objects in Figs 13 and 14 these bulge-dominated morphologies are good fits to the objects. For these star-forming bulges, we have also shown the best-fitting SED models and below them the same best-fitting models this time corrected for the modelled dust obscuration. These dust-corrected SEDs allow a direct comparison between the contribution to the flux of the galaxy at the blue end from the bulge and disc components and have been included as they support the classification of the bulge components as star forming.

Finally, we have also explored the mass and redshift distributions for the entire star-forming bulge-dominated galaxy population, using the overall sSFR $< 10^{-10}\,\mathrm{yr}^{-1}$ and $B/T > 0.5\,H_{160}$ light-fraction criteria to obtain larger numbers for comparison and find that the
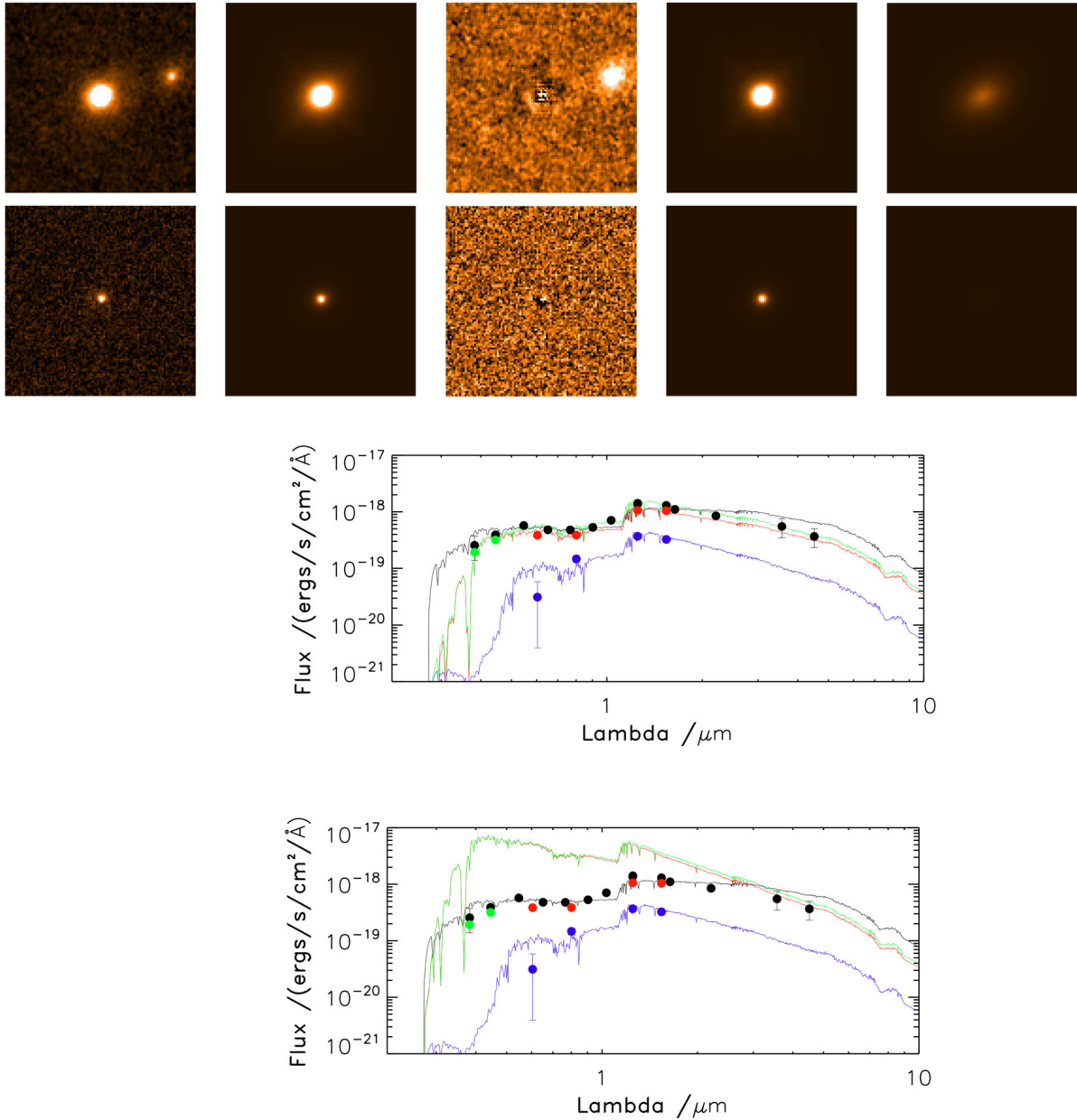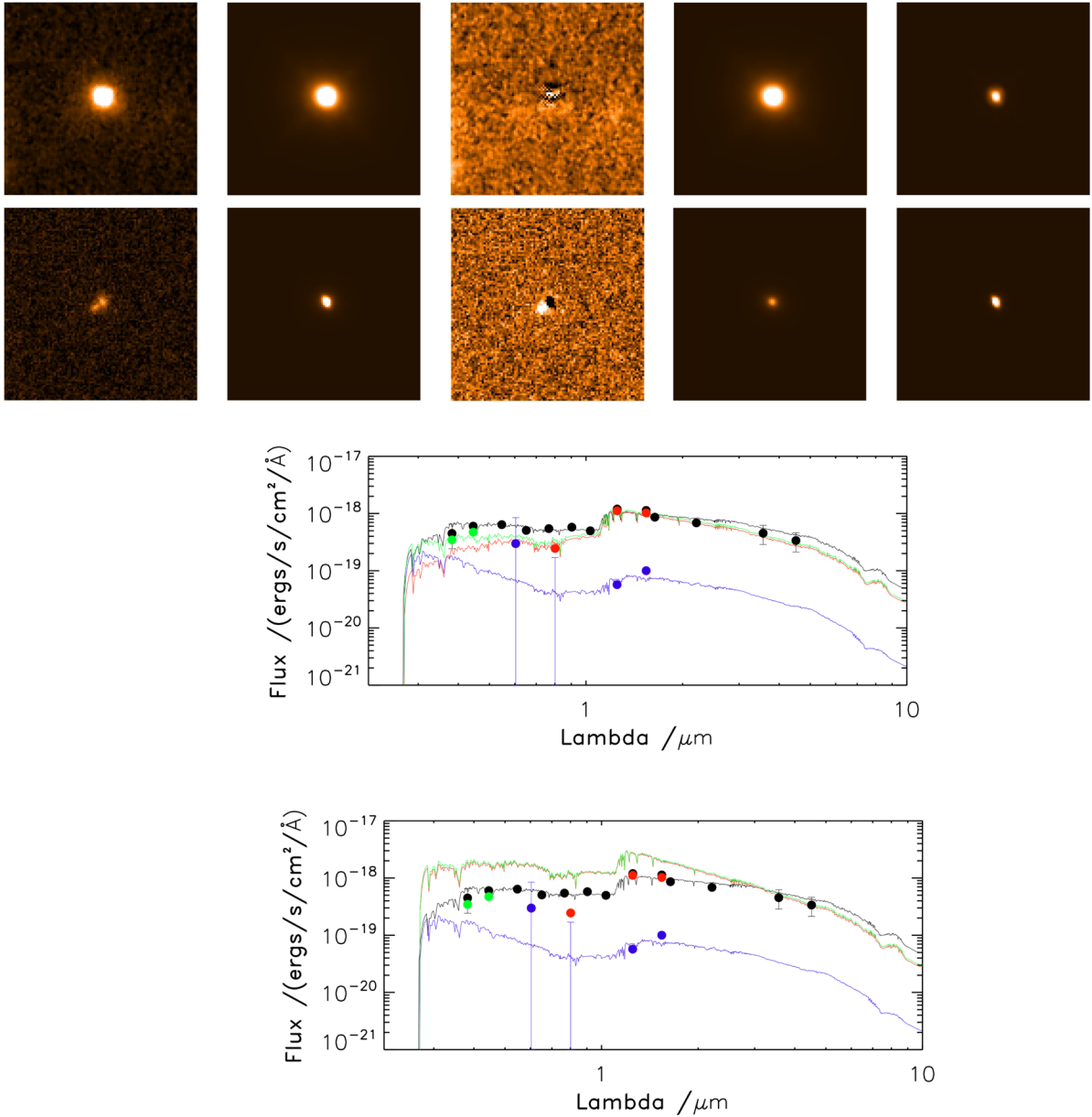
**Figure 13.** The first genuinely star-forming bulge-dominated galaxy in our sample. The first row displays the 6 × 6 stamps for the $H_{160}$ images. From left to right they are the image stamp, the best-fitting multiple-component model, the residual, the bulge component of the best-fitting model and the disc component of the best-fitting model. The second row follows the same configuration for the blue $v_{606}$ stamps. The third row show the best-fitting decomposed SED. The bottom panel shows the dust-corrected best-fitting SED models to allow a direct comparison of the contribution from the bulge and disc components.

star-forming bulge-dominated galaxies appear to preferentially lie at higher redshifts compared to both the full $M_* > 10^{11}\,M_{\odot}$ sample and all bulge-dominated galaxies, see Fig. 15. This result is not statistically significant, which may be due to the small number of objects in the star-forming bulge sample, but a Kolmogorov-Smirnov (K-S) test does reveal that the passive discs and star-forming bulges are not consistent with being drawn from the same distribution at the 3σ level. In fact, given the mass selection imposed for this study, this result is to be expected in the context of downsizing, where the most massive galaxies are observed to be more active at higher redshift and experience an accelerated evolution, quenching before less massive systems. This is further supported by the similarity in the redshift distributions of the star-forming bulges and all star-forming galaxies.

## 7 AXIAL RATIOS

In addition to providing new insight into how the overall morphologies of the star forming and passive components evolve, the detailed morphological analysis employed in this work has also allowed us to explore the axial ratios of the passive and star-forming populations. Axial ratio measurements provide valuable additional information about the structure of these components and any trends with redshift can offer further indicators of the physical processes which govern galaxy evolution within this epoch.

The axial ratio distributions for the disc components of disc-dominated galaxies (as judged by $H_{160}$ light fractions >0.5, which for these purposes does not differ significantly from the decomposed mass fractions) and bulge components of the bulge-dominated

**Figure 14.** The second genuinely star-forming bulge-dominated galaxy in our sample. This figure follows the same configuration as Fig. 13, where in the bottom panels, which illustrate the SED fits, the green data points are the re-measured 2.5 arcsec radius aperture photometry in the $u'$ and $B$ bands.

galaxies are shown in Fig. 16, where the samples have been split into passive and star-forming sub-populations using the total galaxy sSFR at sSFR $= 10^{-10}$ yr$^{-1}$, for simplicity. Similar to the results in Bruce et al. (2012), these distributions reveal that the axial ratios of both the star-forming and passive bulge components are peaked around $b/a \approx 0.7$, consistent with bulges in the local Universe (e.g. Padilla & Strauss 2008). However, visually the passive discs display a markedly flatter distribution to the star-forming discs, which look to be more consistent with the bulge components. Even so, based on the results from K-S tests, all four distributions shown in Fig. 16 are actually consistent with being drawn from the same underlying distribution. This includes the passive and star-forming discs which, despite appearing to be significantly different, are not statistically distinguishable at the $2\sigma$ level ($p = 0.11$).

The peaked distribution of the bulge components is consistent with a population of triaxial objects, and similar distributions have

been found for bulge-dominated systems at both low (e.g. Padilla & Strauss 2008) and high redshifts (e.g. Ravindranath et al. 2006). Similarly, the apparently flatter distribution of the passive discs is in agreement with expectations from a population of randomly oriented thin discs.

### 7.1 Passive discs

The apparently flat distribution for the passive discs provides further corroboration that the passive disc-dominated galaxies are genuine, and agrees well with other axial ratio studies at $z > 1$ such as Chang et al. (2013a). This study used CANDELS photometry to explore the evolution of the axial ratios of early-type galaxies (ETGs) defined by low star formation rates from rest-frame colours, where no additional morphological distinction was made. Chang et al. (2013a) found, from de-projecting the observed axial ratios of the galaxies
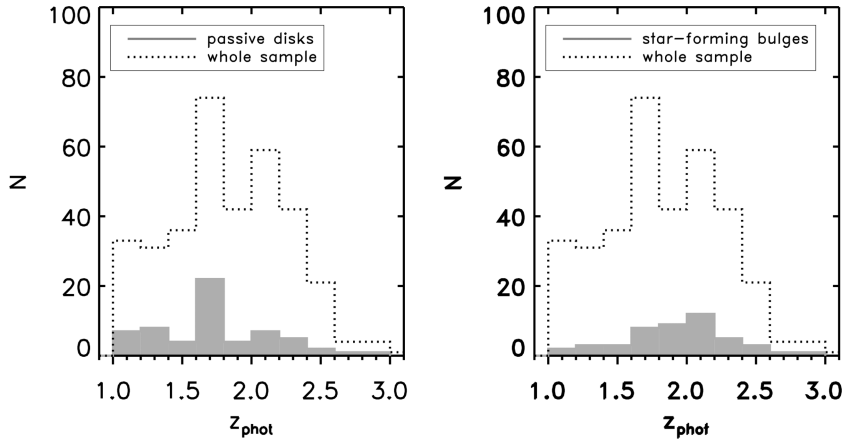
**Figure 15.** The redshift distribution of all the $B/T < 0.5$ passive discs (left) and $B/T > 0.5$ star-forming bulges (right), compared to the whole sample of objects. This appears to show that the star-forming bulges preferentially lie at higher redshifts. This result is not statistically significant, which may be due to the small number of objects in the star-forming bulge sample, but a K-S test does reveal that the passive discs and star-forming bulges are not consistent with being drawn from the same distribution at the $3\sigma$ level.
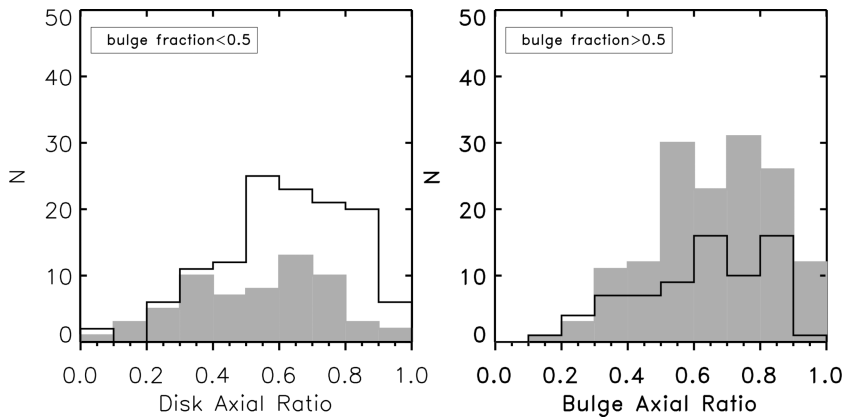


**Figure 16.** Axial ratio distributions for the star forming and passive disc (left) and bulge (right) components of the disc- and bulge-dominated galaxies. In both plots, the star-forming components are plotted in the black solid line, while the passive components are represented by the filled grey regions.

in their sample, that both the local SDSS distribution and their $1 < z < 2.5$ distribution were not consistent with a single population of structures which are randomly oriented, but can be accurately modelled by two components: a round triaxial (bulge-like) population and a flatter oblate (disc-like) population. In their high-mass $M_* > 10^{10.8}$ M$_\odot$ bin, they also found evidence that this oblate population increases as a fraction of the total number of objects from $20 \pm 2$ per cent at $z = 0$ to $60 \pm 1$ per cent at $1 < z < 2.5$. These results not only support the flat distribution that we find for the passive discs but also serve to independently substantiate the findings that, at higher redshifts, these most massive galaxies are increasingly disc-dominated, and that pure bulge galaxies emerge slowly within the $0 < z < 3$ epoch from a population of mixed systems.

Given that Chang et al. (2013a) used single-Sérsic morphological fits, to allow a more direct comparison we have included the single-Sérsic axial ratio fits from our passive discs in the left-hand panel of Fig. 17. Also included in the comparison in Fig. 17 is the model distribution for the local SDSS galaxies from Holden et al. (2012). From this comparison, our passive discs appear to display a distribution which is somewhat intermediate between the peaked local distribution and the $1 < z < 2.5$ ETG sample, which has a more extended flat tail. By explicitly splitting the passive population into the bulge- and disc-dominated samples there is a

more discernible difference between the contribution of the oblate population to the overall axial ratio distribution in the Chang et al. (2013a) models, compared to the distribution of the passive discs in our mass-selected sample. From this comparison, the extended flat tail from discs appears more populated in the Chang et al. (2013a) models than with respect to our observed distributions, especially at $b/a < 0.35$. However, there are still visual indications that the passive discs have a flatter distribution than the star-forming discs, although these are not statistically significant. Thus, both our single-Sérsic and morphologically decomposed results broadly agree with the results of Chang et al. (2013a), especially given the difference in the mass ranges adopted.

Chevance et al. (2012) have also explored the axial ratios of 31 compact ($R_e < 2$kpc), passive galaxies at $z > 1.5$ and find that while the single-Sérsic index distributions of their high-redshift sample are more consistent with local discs, the axial ratio distribution has only a 5 per cent probability of being drawn from the same population and is more consistent with the distribution of local ETGs. These results suggest that despite the passive galaxies having 'disc-like' light profiles, their axial ratios are rounder. Chevance et al. propose that their high-redshift sample is either a mixture of bulges and discs or that the high-redshift galaxies are a genuinely distinct population with no real local analogues. By cutting our full sample at $z > 1.5$
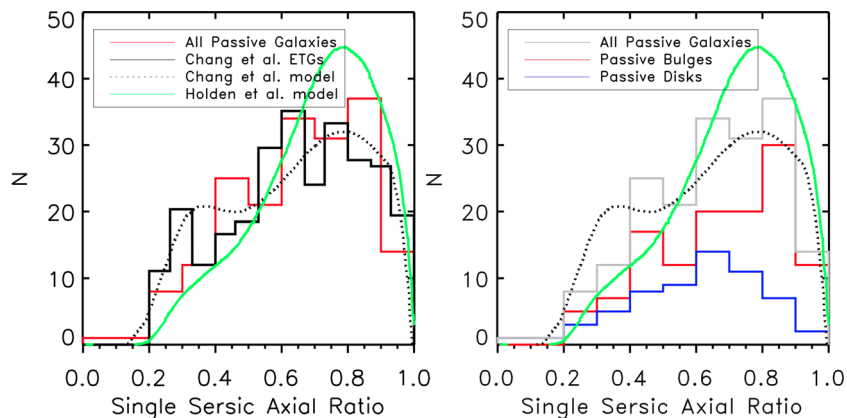
**Figure 17.** Left: the single-Sérsic axial ratio distributions for the passive (red) galaxies in our sample overplotted with the Chang et al. (2013a) observed distribution in black and their model in the dotted black line, where these distributions have been re-normalized to match the area under our histograms. Also included in this plot is the local SDSS model distribution from Holden et al. (2012). The passive galaxies in our mass-selected sample display a distribution which appears to be intermediate between the $1 < z < 2.5$ Chang et al. (2013a) ETGs, and the local SDSS sample. Right: the axial ratio distributions from the single-Sérsic fitting for the passive galaxies (grey) also split into the bulge- (red) and disc-dominated (blue) populations. By splitting the passive galaxies into their morphological classifications, we find that the single-Sérsic axial ratios also separate into a flatter distribution for the oblate disc-dominated objects and a peaked distribution for the triaxial bulge-dominated galaxies. This is roughly consistent with the Chang et al. (2013a) results, although the contribution from the oblate population in the models of Chang et al. (2013a) to the flat tail of the distribution appears to be significantly larger in comparison with our sample.

and plotting the single-Sérsic index and axial ratio distributions of all the passive galaxies and just the most compact systems with $R_e < 2$kpc, we find agreement with the Chevance et al. (2012) results. The single-Sérsic index distributions are more similar to the distributions of local discs than ETGS, peaking at a value of $n \sim 1.5-2$, while the axial ratio distributions are more peaked than the flat distributions observed from local discs. In fact, examining the bulge-to-total light fractions from our decompositions reveals that these passive, compact, objects are indeed a mixture of bulge plus disc systems with a median $B/T \sim 0.59$. These results are in line with our previous findings that within the $1 < z < 3$ era all massive galaxies become increasingly mixed systems, which gives rise to measured single-Sérsic indices which have intermediate values.
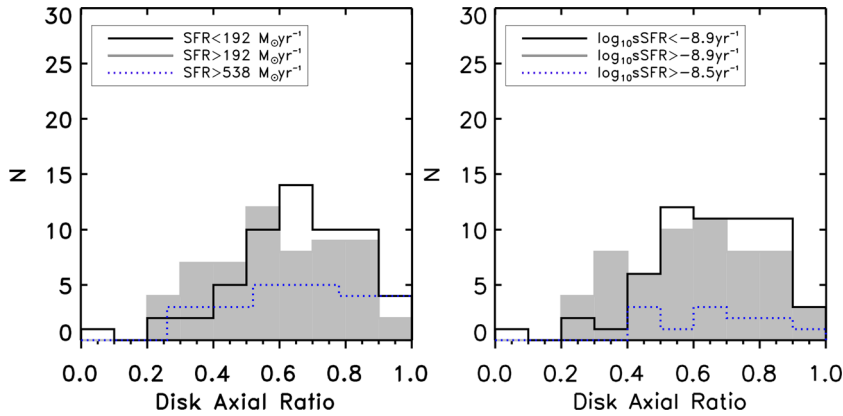
### 7.2 Star-forming discs

While the flat distribution of the passive disc components is supported by previous studies, the relatively peaked distribution of the star-forming disc components has been less well explored in the literature, and remains less understood. Nevertheless, this peaked distribution does agree with the results of Law et al. (2012), who conducted a single-Sérsic and non-parametric morphological analysis of $M_* = 10^8-10^{11}$ M$_\odot$ star-forming galaxies at $1.5 < z < 3$ using *HST*/WFC3 imaging and reported an axial ratio distribution for $n < 2.5$ galaxies peaked at $b/a \approx 0.6$.

To better explore the origin of this peaked distribution, we have cut our star-forming, disc dominated, disc component sample according to several different criteria. In the first case, we have cut the sample according to different indicators and measures of star formation. We first compared the axial ratio distributions of the whole star-forming disc-dominated population with only those objects which also had a 24 μm detection from either SpUDS or S-COSMOS. However, this was not informative as the majority of star-forming disc-dominated galaxies have a 24 μm counterpart. We next compared the distributions for the sample split by their absolute and sSFRs, as shown in Fig. 18. The left-hand panel of Fig. 18 displays the cuts made at increasingly higher absolute star formation rates for the overall galaxy. The SFR $> 190$ M$_\odot$ yr$^{-1}$ cut corresponds

to the median absolute star formation rate for the full star-forming disc-dominated galaxy sample, and the SFR $> 540$ M$_\odot$ yr$^{-1}$ cut corresponds to the 90th percentile value. There is perhaps tentative evidence from this comparison that by imposing the extreme SFR cut, the distribution begins to flatten out, however the number of galaxies within this bin becomes very small, so this result is by no means robust. The right-hand panel of Fig. 17 displays similar cuts made at increasingly higher sSFRs for the overall galaxy. The sSFR $> 10^{-8.9}$ yr$^{-1}$ cut now corresponds to the median sSFR for the full star-forming disc-dominated galaxy sample, and the sSFR $> 10^{-8.5}$ yr$^{-1}$ cut corresponds to the 90 per cent quartile value. These distributions agree with the results from splitting by absolute star formation rate as they also display a weak trend for the most active discs defined by sSFR to have flatter axial ratios.

In addition to studying how the axial ratio distribution of the disc components varies with the star formation rate of the galaxy, we have also examined how it varies with other properties of the galaxy. To do this, we first split the star-forming, disc-dominated, disc components above and below $z = 2$ to investigate if there was any redshift evolution evident. These distributions are given in the left-hand panel of Fig. 19, and reveal that the star-forming disc components at $z > 2$ are peaked towards a higher $b/a$ value compared to the $z < 2$ components. This is interesting as, naively the $z > 2$ discs would be expected to be more active than those at $z < 2$. Given that for the previous figure, we reported that there might be a potential trend for the distribution to flatten out for the most active discs, this result appears to be in direct conflict with this assertion. Moreover, we have also conducted a K-S test for these two redshift binned distributions and found that at the $2\sigma$ level ($p = 0.02$) they are inconsistent with being drawn from the same distribution. However, in addition to a star formation rate evolution with redshift, we have also reported on the size evolution of the bulge and disc components with redshift in Bruce et al. (2013b), so in the right-hand panel of Fig. 19 we have split the discs according to their median size. This clearly reveals that the largest discs have a flatter distribution and the smaller discs have a distribution peaked towards higher values. In this case the K-S test provides a value of $p = 0.03$, again making them formally different at the $2\sigma$ level.

**Figure 18.** Axial ratio distributions for the star-forming discs split by different measures of specific and absolute star formation rate. On the left, the star-forming discs have been split at the median absolute star formation for the galaxies in this sub-population and the two distributions have been plotted with the less active star-formers in black and the more active discs in grey. We have also constructed an additional sub-sample of objects which have SFRs above the 90th percentile and have overplotted the axial ratios of their disc components in blue. This comparison appears to show tentative evidence that the most active discs have a flatter axial ratio distribution. On the right, the star-forming discs have been split at the median specific star formation for the galaxies in this sub-population and the two distributions have been plotted with the less active star-formers in black and the more active discs in grey. We have also constructed an additional sub-sample of objects which have sSFRs above the 90th percentile and have overplotted the axial ratios of their disc components in blue. This comparison appears to also show some weak evidence that the most active discs have a flatter axial ratio distribution.
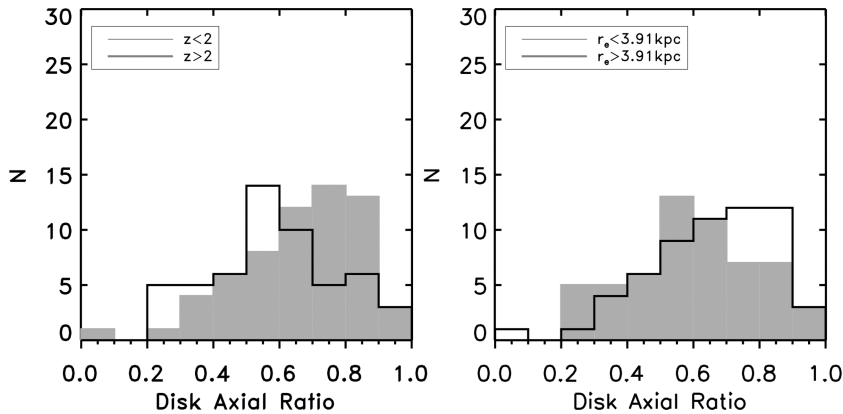


**Figure 19.** The axial ratio distributions for the star-forming discs split by photometric redshift (left) and disc size (right), where the discs have been split according to the median disc size of 3.9 kpc. These distributions reveal a trend for lower redshift galaxies to have flatter axial ratios, although this can be explained by the redshift size evolution of the discs. In fact, these distributions demonstrate that the smallest discs are the most triaxial, which may be due to an absolute increase in disc scaleheight due to star formation at high redshift which would have a greater effect on the axial ratios of discs with smaller scalelengths.

The trend for smaller star-forming discs to be rounder and larger discs to be flatter can be explained if at these redshifts star formation in discs depends only on the self-gravity of the disc, not on scalelength, and this intense star formation phase induces feedback which 'puffs up' the disc scaleheight. In which case, the 'puffiness' of the star-forming disc is independent of the disc size, and smaller discs will appear more triaxial in structure than larger discs. Alternatively, if these high-redshift discs are clumpy then it possible that an increase in scaleheight may be driven by asymmetries, but the star-forming clumps in high-redshift discs have been found to not contribute significantly to the near-infrared flux (Wuyts et al. 2012), where our morphological decompositions are based.

For completeness, we have also ensured that these trends are not biased by also selecting only the disc components of disc-dominated galaxies as classified by their decomposed disc/bulge+disc masses and by splitting the sample by disc decomposed mass above and below the median value of $M_{\mathrm{disc*}}$.

It is worth noting that previous studies and GALFIT simulations have expressed some concern about the robustness of GALFIT results for small, flat objects due to the resolution limit, where $b/a \leq 0.1$ values of small objects result in scaleheights less than a single pixel (van der Wel et al. 2012 and private communication). Having explored this with our own simulation results, we also find evidence that the single pixel effective radius disc models with axial ratios 0.1 are not well recovered and axial ratio distribution of the best fits is centred on $b/a = 0.05$ with a secondary, small, peak in the distribution at $b/a = 0.2$. Such offsets are not witnessed for small disc models with $b/a = 0.3$, 0.6 or 1.0, nor for our disc models with effective radii of 5 or more pixels, but in which cases there is a slight tail in the fitted $b/a$ distributions towards higher $b/a$ values such that the recovered fits for the $b/a = 0.1$ models are not symmetric. (For completeness, examination of the fitted axial ratios with $b/a >$ 0.1 for larger model discs also show no offsets but have slightly less spread in the fitted $b/a$ distributions, which shows that for $b/a >$
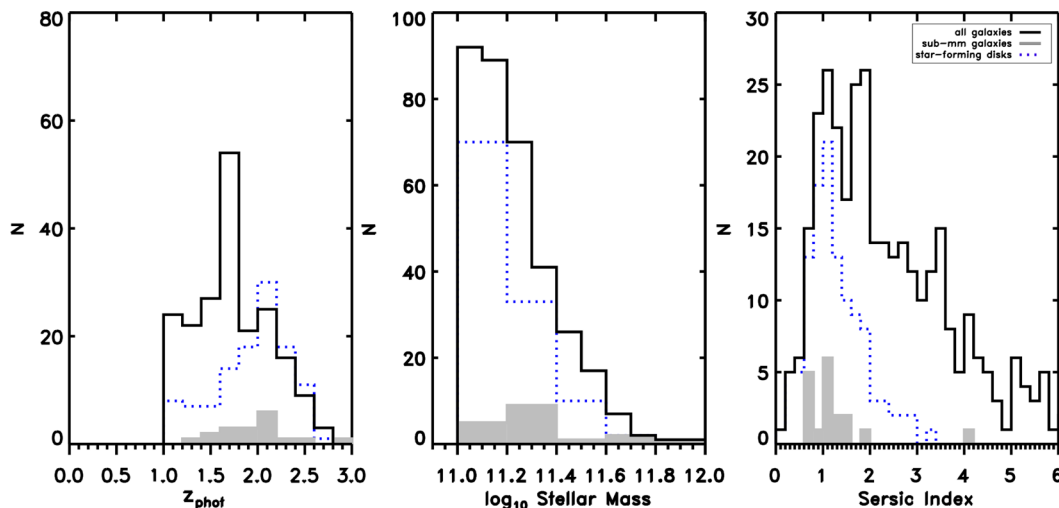
**Figure 20.** Comparison of the properties of our sample and the mass-selected sample of Targett et al. (2013). The combined UDS and COSMOS CANDELS samples are plotted in the black solid histograms and the star-forming disc-dominated galaxies in the blue dashed histograms, where here the properties for the overall galaxies rather than for the disc components are used to allow a fairer comparison to the (sub-)mm selected samples. The Targett et al. (2013) (sub-)mm sample is shown in the light grey filled histogram. The left-hand panel displays the redshift distributions, the middle panel shows the total galaxy stellar mass distributions and the right-hand panel shows the single-Sérsic index distributions. The comparison between these samples verifies that the GOODS-S and AzTEC (sub-)mm sample contains comparably massive, disc-dominated galaxies at similar redshifts to our CANDELS galaxies.

0.1 1 pixel disc models the fitting procedure is not biased but does carry a larger random uncertainty.)

However, this is clearly not the reason for the dearth of $b/a < 0.3$ values for the star-forming discs within our sample, as not only are the sizes of our objects too large to force the scaleheights of the majority of $b/a$ fits to be less than a pixel, but if this were the case then we would have found an overabundance of $b/a < 0.1$ values, which is not seen.

## 8 COMPARISON WITH SUB-MM GALAXIES

One of the main insights from this work is that the disc components of the star-forming disc-dominated galaxies have surprisingly peaked axial ratio distributions but that we find tentative evidence that the most active star-forming galaxies have the flattest distributions. However, in order to isolate the most active systems, we restricted this cut to a very small number of objects, which prevented us from drawing any robust conclusions. As a result, this issue is clearly worthy of further investigation. To this end, in this section we have considered the mm/sub-mm AzTEC selected sample of Targett et al. (2013) in the GOODS-South field, which has been selected from sub-mm imaging at a uniform depth over a similar area to the CANDELS-UDS and COSMOS fields. Sub-mm selected galaxies are widely agreed to be extreme star-forming galaxies, although there is debate over whether this activity is triggered by major mergers or whether it is just the high-end tail of the normal star formation main sequence. One of the main conclusions of Targett et al. (2013) is that the (sub-)mm selected galaxies represent the extreme star-forming end of the morphologically disc-dominated population, thus they provide the ideal sample for extension of this axial ratio study.

First of all, in order to ascertain how valid a comparison is between our star-forming discs and the (sub-)mm galaxy sample, we have compared the properties of the samples in Fig. 20. Our entire mass-selected galaxy sample is plotted in black, our star-forming discs are plotted in blue, and the (sub-)mm galaxies are plotted in light grey. This colour scheme is adopted for all subsequent figures.

The far left-hand panel of Fig. 20 shows the photometric-redshift distributions of the samples, and confirms that the (sub-)mm galaxies span the full extent of the redshift regime covered by our study. The mass distributions of the samples are plotted in the middle panel of Fig. 20, and reveal that the (sub-)mm selected sample provide a comparable sample for an extreme population with similar stellar masses to our purely mass-selected sample. The last panel of Fig. 20 shows the distribution for the single-Sérsic indices of the samples. It should be noted here that the study of Targett et al. (2013) was conducted using both a single-Sérsic index morphological fit and a detailed decomposition of the individual clumps in each (sub-)mm galaxy, but it is the overall single-Sérsic index results which are used here and compared with our single-Sérsic index fits.
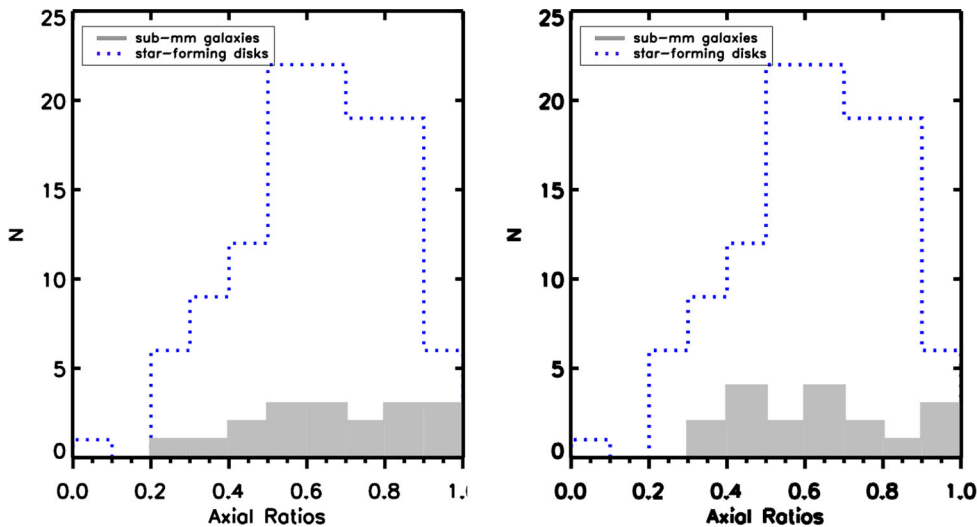
Finally, as we have previously found that the axial ratios of the star-forming discs depends on the size of the disc components, in Fig. 21 we have also compared the size distributions for the overall galaxies, again to provide the most direct comparison of the whole galaxy we use sizes estimated from the single-Sérsic fits. This shows that the (sub-)mm galaxies span roughly the same size range as our star-forming disc-dominated galaxies.

Having verified that the (sub-)mm selected galaxies provide a legitimate sample with which to conduct a direct morphological comparison between the 'normal' star-forming galaxies in our CANDELS study and an extreme star-forming population, we have examined the axial ratio distributions for the different populations and have plotted them in Fig. 22. For the above comparisons, which were included to establish the validity of the morphological comparison between the near-IR and (sub-)mm selected samples, we have used the properties of the overall galaxies. In most cases these properties correspond to genuinely disc-dominated star-forming objects and so a direct comparison between the overall galaxy axial ratios for the (sub-)mm selected sample and the distributions for the disc components of our star-forming disc-dominated objects is justifiable. However, Targett et al. (2013) conducted a decomposition of the individual clumps, so in Fig. 22 we have overplotted the axial ratio distributions from the disc components of the star-forming disc-dominated CANDELS sample with the distributions from the
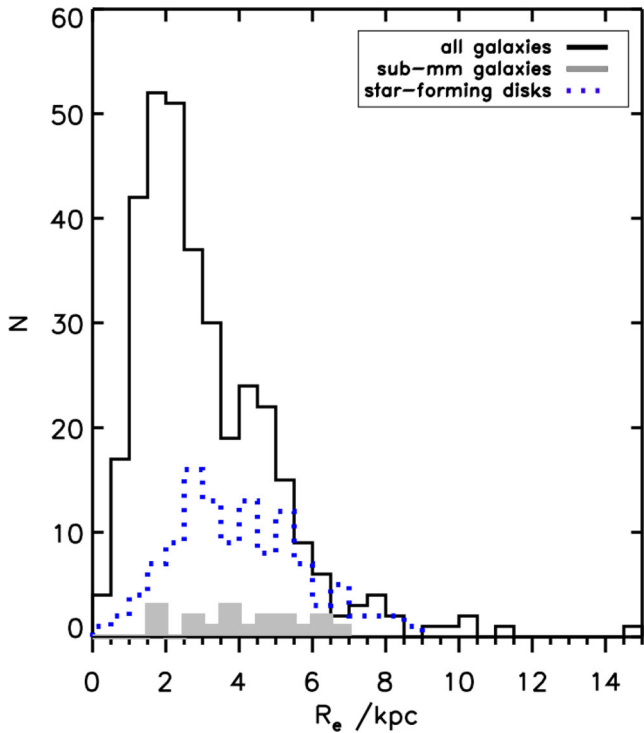
**Figure 21.** Size distributions of the CANDELS galaxies (black = all galaxies, blue = star-forming discs), overplotted with the size distributions of the (sub-)mm galaxies (grey). This shows that the (sub-)mm selected galaxies span roughly the same size range as our star-forming disc-dominated galaxies.

single-Sérsic model of the (sub-)mm galaxies in the left-hand panel, and with the primary (flux dominant) component of the decomposed model of the (sub-)mm galaxies in the right-hand panel, even in the case where the primary clump was best fitted with an $n > 2.5$ profile (which will only result in a more peaked distribution).
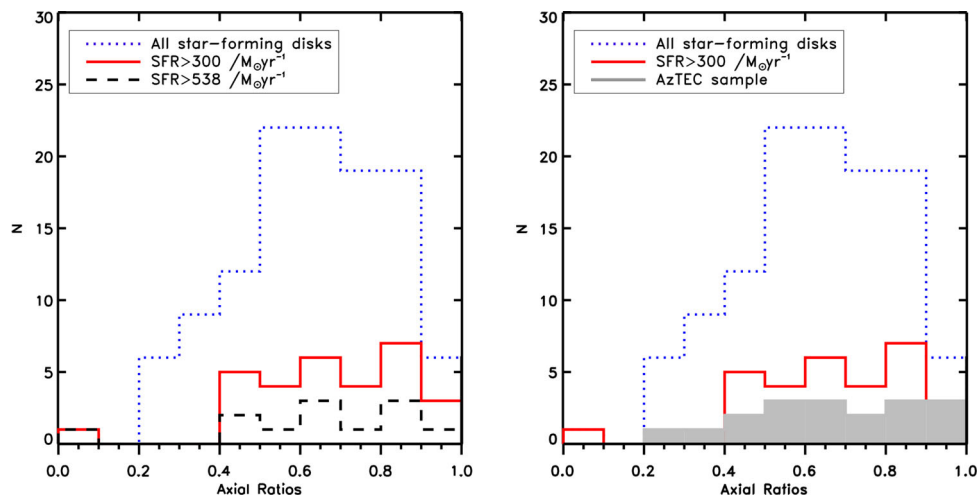
In fact, comparison of the axial ratio distributions reveals that the distributions for the (sub-)mm galaxies are flatter than for our star-forming disc components, which lends further support to our previous, tentative, findings that the axial ratio distribution of the most active star-forming galaxies appears to flatten out. The statistics for this comparison are weak, but this apparent trend allows speculation that if there is a maximum surface density of star formation at high redshift, then the most star-forming discs, will also be expected to be the largest, which agrees with the other observed trend between larger sizes and flatter axial ratio distributions and so goes some way to delivering at least a self-consistent picture of star-forming high-redshift discs.

We have also explored cutting our sample at a star formation rate that roughly matches the surface number density of the (sub-)mm galaxy sample. Allowing for the survey areas this match in surface number density is achieved at SFR $> 300\,\mathrm{M_\odot\,yr^{-1}}$. A comparison between the axial ratios of our full star-forming disc sample, the SFR $> 300\,\mathrm{M_\odot\,yr^{-1}}$ sub-set and the previously flat distribution for the extreme SFR $> 538\,\mathrm{M_\odot\,yr^{-1}}$ (90 per cent quartile) cut is given in the left-hand panel of Fig. 23. The whole star-forming disc sample and the SFR $> 300\,\mathrm{M_\odot\,yr^{-1}}$ sub-set are also directly overplotted with the axial ratio distributions for the (sub-)mm selected sample in the right-hand panel of Fig. 23. This further demonstrates that, by selecting the most active star-forming discs, comparable to the extreme star-forming (sub-)mm selected sample, the axial ratio distributions appear, comparably flat (although statistics from a K-S test are inconclusive).

## 9 DISCUSSION

By exploiting our decomposed stellar mass and star formation rate estimates, we have been able to better explore the evolution of the full range of morphological properties exhibited by our massive, high-redshift galaxy sample.

The most fundamental morphological measurement is the relative dominance of the bulge and disc components, as measured in terms



**Figure 22.** The axial ratio distributions of the (sub-)mm galaxies, where again the (sub-)mm selected sample is in light grey. The (sub-)mm selected sample was modelled in Targett et al. (2013) using both a single Sérsic fit and multiple component fits to each clump. Therefore, on the left we have plotted the axial ratio distributions from the single Sérsic fits and in the right-hand plot the distributions for the axial ratios of the flux-dominant component/clump, even in the case where that component was best fitted with $n > 2.5$. In both plots the axial ratio distributions for the (sub-)mm selected galaxies are considerably flatter than the distributions for the CANDELS star-forming discs. Although the numbers within the sample are too small for a robust statistical comparison, it does appear that the trend for the axial ratios of the most actively star-forming galaxies to flatten-out extends to the extreme star-forming (sub-)mm selected population.

**Figure 23.** Left: the axial ratio distributions of all the star-forming discs in our sample (blue dotted histogram), the sub-set cut at a similar star formation rate (SFR > 300 $M_\odot$ yr$^{-1}$) as the (sub-)mm AzTEC selected sample (red solid histogram), and the extreme 90th percentile cut imposed previously (black dashed histogram). Right: the axial ratio distributions of all the star-forming discs (blue) and the SFR > 300 $M_\odot$ yr$^{-1}$ sub-set (red), overplotted with the distributions for the (sub-)mm AzTEC selected sample (grey filled histogram). This further demonstrates that by selecting the most active star-forming discs, comparable to the extreme star-forming (sub-)mm selected sample, the axial ratio distributions appear comparably flat.

of the galaxy morphology from the light fractions and by their contribution to the total galaxy mass. Here, although we continue to find a decrease in the fraction of disc-dominated objects from $z = 3$ to 1, we also see that the evolution of bulge dominated, and essentially 'pure' bulges ($B/T > 0.9$, where our $B/T$ ratios are accurate to within ~10 per cent), is relatively slow. The decrease in disc-dominated objects is instead accompanied by an increase in mixed bulge+disc systems with decreasing redshift, where, by incorporating the decomposed stellar mass results, we find that this morphological evolution is accompanied by an increase in the bulge component mass of the objects.

These results suggest that, instead of a clear transition at $z = 2$ when the most massive galaxies transform straight from disc- to bulge-dominated systems, at $1 < z < 3$ there is a more gradual emergence of a mass-dominant bulge component while the galaxies still display a mixed bulge+disc morphology. Even by $z = 1$ these massive galaxies do not display the 'pure' bulge morphologies exhibited by >60 per cent of similarly massive galaxies in the local Universe (Buitrago et al. 2013a), and in fact may be more comparable to local S0 galaxies.

At high redshifts, an increased fraction of massive disc-dominated galaxies is in agreement with previous studies, covering similar mass and redshift regimes, such as Buitrago et al. (2008), Conselice et al. (2011) and Buitrago et al. (2013a). In addition to these studies, Mortlock et al. (2013) have conducted visual morphological classifications of $M_* > 10^{10}$ $M_\odot$ galaxies at $1 < z < 3$ using CANDELS WFC3/IR imaging. For comparison, Mortlock et al. (2013) find that classifying bulges and discs by the $n = 2.5$ cut returns a morphological evolution for their highest mass bin ($M_* > 10^{10.5}$ $M_\odot$) in agreement with our findings, whereby there is a transition from bulge- to disc-dominated morphologies at $z \sim 2$. However, their visual classification suggests that, even for this high-mass bin, the fraction of bulge- and disc-dominated systems increases with decreasing redshift, and is accompanied by a fall in the fraction of 'peculiar' morphologies. This may be explained if, at high redshift, star-forming discs have not yet relaxed into stable discs and display disturbed and/or interacting morphologies. We note that although ~80 per cent of the disc-dominated objects

within our sample were well fitted by the symmetric profiles, the remaining fraction required re-fitting with additional masking to achieve acceptable fits. Despite the fact that the underlying profiles of these re-fitted objects were disc-like exponentials, the additional structure (whether clumps, spiral features or other asymmetries) may influence visual classifications.

In addition to the morphological evolution with redshift, our analysis of the star formation activity in the bulge and disc components has also delivered new insights into the evolution of the massive galaxies within our sample. One of the most interesting results from recent morphological studies has been the discovery that a significant fraction of passive galaxies are in fact disc dominated, and star-forming galaxies are bulge dominated. Star-forming bulges and passive discs have been previously observed at both high and low redshift, however the large fractions found within the sample of Bruce et al. (2012) were unexpected. By effectively doubling the sample size (by combining the CANDELS-UDS and COSMOS samples), the reported fractions from Bruce et al. (2012) have been further substantiated and we find that using the *overall* galaxy star formation rates from SED fitting as discriminators (which correlate extremely well with UVJ classifications of passive and star-forming) ~30 per cent of all star-forming and passive galaxies are bulge- and disc dominated, respectively.

Several other recent studies have also found higher fractions of passive disc-dominated galaxies (the majority of which can potentially contain a bulge component at some level), more comparable to the ~30 per cent quoted here. In particular, Wang et al. (2012) report a passive, visually-classified, disc-dominated fraction of ~30 per cent for $M_* > 10^{11}$ $M_\odot$ at $1.5 < z < 2.5$; Lee et al. (2013) have published broadly consistent results from non-parametric and single-Sérsic fitting for their 35 $1.4 < z < 2.5$ passive galaxies (although note the low S/N of these sources); McLure et al. (2013) find a passive, single-Sérsic determined, disc-dominated fraction of $44 \pm 12$ per cent for their $M_* > 6 \times 10^{10}$ $M_\odot$, $1.3 < z < 1.5$ sample; van der Wel et al. (2011) extrapolate from the 14 galaxies with $M_* > 10^{10.8}$ $M_\odot$, $1.5 < z < 2.5$ in their sample, based on visual, Sérsic decomposition and axial ratio results, that $64 \pm 15$ per cent of all high-redshift passive galaxies are disc dominated; and Fan et al.

(2013) find that $68 \pm 24$ per cent of the 19 passive $z \approx 3$ galaxies in their sample are disc dominated with $n < 2$ and with consistently flat axial ratios.

However, we have also discussed how these statistics may be biased due to the use of star formation rate estimates for the whole galaxy rather than for the individual bulge and disc components. To this end, we re-evaluated the fractions of galaxies in our sample in each population using the strictest criteria possible in terms of both star formation rate and component dominance. This conservative approach revealed that only $\sim 18 \pm 5$ per cent of passive galaxies are disc dominated and $\sim 11 \pm 3$ per cent of star-forming galaxies are bulge dominated by the $H_{160}$-band morphology and by mass.

The gradual emergence of a mixed bulge+disc (but increasingly bulge-dominated) population at $1 < z < 3$, coupled with the discovery of a significant population of both star-forming bulges and passive discs, reveals that while in most cases bulge growth and quiescence are correlated, there is significant scatter, suggesting that the physical processes which quench these massive galaxies are not simply connected to the mechanisms which bring about the morphological transitions witnessed within this era.

While major gas-poor mergers between $1 < z < 3$ can account for the transition of disc-dominated to bulge-dominated systems (Robertson et al. 2006), this process is fairly rapid and appears at odds with the gradual emergence of increasingly bulge dominated revealed by our study. The model of VDI is more consistent with the morphological evolution displayed by the galaxies within our $1 < z < 3$ sample. The VDI scenario has gained increasing support from both recent simulations and observations. This model proposes that, in high-redshift star-forming discs, massive clumps form from gravitational instabilities within the disc. These clumps then migrate towards the centre of the disc transferring gas and stars to the centre of the system and build a bulge component. There is significant observational evidence of star-forming clumps within high-redshift discs from, for example, Elmegreen & Elmegreen (2005), Elmegreen et al. (2009), Guo et al. (2011), Wuyts et al. (2012) and Mozena et al. (in preparation). These studies agree that $\sim 70$ per cent of massive $1 < z < 3$ star-forming galaxies contain at least a few kpc-sized star-forming clumps. In fact Elmegreen et al. (2009) claim that, within these discs, the contribution to the total star formation rate is split equally between the clumps and the diffuse disc. The formation and migration of giant clumps within a gas-rich disc can be well modelled (e.g. Ceverino et al. 2010; Martig et al. 2012; Hopkins et al. 2012), as can the formation of a central bulge and the reshaping of the remaining disc to an exponential density profile (e.g. Bournaud, Elmegreen & Elmegreen 2007; Krumholz & Burkert 2010; Bournaud et al. 2011). However, there is some debate over the extent to which these clumps can survive or reform after disruption from feedback, and whether they can survive long enough to migrate to the centre of the discs (e.g. Genzel et al. 2011; Hopkins et al. 2012).

The latest simulations (for example Bournaud et al. 2013; Dekel & Krumholz 2013) address this issue by modelling the effects of photoionization, radiation pressure and supernova feedback on the clumps and find that, in their models, the clumps can account for any momentum-driven mass outflows and tidal stripping of gas and stars by re-accreting from the gas-rich disc, so that they maintain constant masses and star formation rates for a few hundred Myr, which is long enough to complete their migration to the centre to merge to form a bulge. However, there remains observational debate (e.g. Elmegreen et al. 2009; Wuyts et al. 2012) over whether the masses in these clumps are actually sufficient to build a central bulge.

The VDI model could plausibly account for the morphological trends observed from our analysis. However, the clump migration mechanism acts to build a central star-forming bulge. It is unclear what becomes of these star-forming central bulges, as this work has found evidence for only a small sub-set of star-forming galaxies which are bulge dominated, where these systems also tend to be at higher redshifts.

Despite the growing evidence for a correlation between star formation quenching and the build-up of a massive bulge displayed by the majority of objects from this and other studies, and debate over whether the witnessed trends can be attributed to major mergers, the presence of passive discs and star-forming bulges is inconsistent with the idea that bulge growth and quenching are simply linked by single process. Thus, these sub-populations suggest that the gas-poor major mergers at $1 < z < 3$ are not solely responsible for both morphological transformations and quenching. There are several competing quenching mechanisms which would not necessarily alter the morphologies of the systems or do so through a less stochastic processes than gas-poor mergers. These include quenching through AGN feedback, halo quenching (e.g. Birnboim & Dekel 2003; Kereš et al. 2005; Dekel et al. 2009a), strangulation (e.g. Skibba et al. 2009) and morphological quenching (e.g. Martig et al. 2009). The VDI model is also consistent with the presence of passive discs if the clump migration which builds a central bulge, but leaves a massive disc in place, is accompanied by morphology quenching in the disc. However, given the reduction in the fraction of genuinely passive discs and star-forming bulges from our full decomposition analysis, it remains to be seen if these models can account for the population statistics.

Finally, in addition to the bulge and disc dominance, and star formation activity of the individual components, we have also explored the difference between the axial ratio distributions of the sub-populations comprising our sample. We found that the axial ratios of the passive discs of disc-dominated galaxies display a flat distribution, consistent with a population of randomly oriented thin discs, whereas the distribution for the star-forming discs is peaked at $b/a \sim 0.7$, consistent with a more triaxial population.

The flat distribution for the passive discs agrees with both the distributions of local discs and the results from van der Wel et al. (2011) and Chang et al. (2013a). Chang et al. (2013a) explored the axial ratio distributions of local and $z \sim 2.5$ ETGs identified on the basis of low star formation rates from rest-frame colours. By deprojecting the observed axial ratios, Chang et al. (2013a) found that the low- and high-redshift ETG samples comprise two populations: triaxial objects, and flatter disc-like galaxies. The identification of disc-like galaxies within the Chang et al. (2013a) ETG sample by axial ratio distributions (which are similar to the distribution for our passive discs) independent of Sérsic index or bulge/disc ratios, helps to confirm that there is a significant population of passive, genuinely disc-dominated galaxies at $z > 1$.

As well as the flat distribution for the passive discs, our two-component analysis has also revealed that the star-forming discs have a distribution more similar to that of the bulges, peaked at $b/a \sim 0.7$ and with a relative dearth of objects with $b/a < 0.3$. Having explored how the axial ratio distribution varies with size and star formation rate, we found that the smaller galaxies tend to be rounder, and the most star-forming galaxies flatter. Due to the small number of objects in our most active star formation rate cut, we also compared our axial ratio distributions to those for (sub-)mm galaxies which are expected to be extreme star-formers, and found that this trend also holds for the more extreme (sub-)mm population. These results lead us to speculate that, at high redshift, feedback

from star formation in discs acts to 'puff-up' their scaleheights, which accounts for the peaked axial ratio distribution of the discs with smaller scalelengths and the flatter axial ratios of larger discs. However, we note that, given in the local Universe systems such as pseudo-bulges or dwarf spheroidals which are not flattened rotating discs can display low Sérsic indices, the true structure of these high-redshift galaxies may also be similarly complex.

## 10 CONCLUSIONS

We have decomposed the most massive ($M_* > 10^{11}\,M_\odot$) galaxies at $1 < z < 3$ in the CANDELS UDS and COSMOS fields into their separate bulge and disc components across multiple bands based on their *HST* WFC3 $H_{160}$-band morphologies. By extending this analysis to conduct individual-component SED fitting, we have been able to estimate decomposed bulge and disc stellar mass and star formation rate estimates. This decomposition analysis has provided us with new insight into the morphological and star formation evolution of these systems.

By comparing the dominance of the bulge and disc fractions in terms of both the $H_{160}$ light fractions and the stellar mass contributions, we find that, within the $1 < z < 3$ redshift era, these most massive galaxies are more disc dominated at higher redshifts and become increasingly mixed bulge+disc systems with decreasing redshift, where they are more bulge dominated by mass than by light. However, even at $z = 1$ the 'pure' bulges comparable to the giant ellipticals have yet to emerge.

Despite confirmation that the colour-morphology bimodality is already well established at $1 < z < 3$, our simple *overall* galaxy sSFR and $H_{160}$-band light fraction classifications have identified a significant fraction of passive galaxies which are disc dominated ($33 \pm 5$ per cent) and star-forming galaxies which are bulge dominated ($29 \pm 5$ per cent). These results challenge the idea that major mergers are the main mechanism for galaxy quenching as the gas-poor major mergers at $1 < z < 3$ would both quench these systems and transform their morphologies from disc- to bulge dominated. In order to better probe this population, we have examined the decomposed stellar mass and star formation rate estimates for the passive discs and star-forming bulges adopting the strictest possible criteria. We conclude that, in fact, only $18 \pm 5$ per cent of passive galaxies are genuinely disc dominated and $11 \pm 3$ per cent of star-forming galaxies are bulge dominated. Both these fractions are significantly lower than the fraction determined from the overall galaxy sSFRs and stellar masses reported by previous studies at similar redshifts and masses, which clearly illustrates the advantage of the full SED decompositions over and above single model fits for this type of analysis.

Nevertheless, the confirmation of a significant population of passive discs and star-forming bulges, coupled with the observed gradual emergence of increasingly mixed bulge+disc systems, with larger bulge/total mass fractions, from $z = 3$ to 1 suggests that, whilst some of these most massive galaxies may undergo major mergers which both quench their star formation and transform their morphologies, there must also be other physical processes which quench star formation but leave a massive disc intact. This evolutionary scenario is more consistent with the models of AGN quenching, halo quenching (Dekel & Birnboim 2006; Dekel et al. 2009a) or possibly VDI (Dekel et al. 2009b; Ceverino et al. 2010).

Finally, in addition to studying the overall morphologies and star formation rates of the most massive galaxies at $1 < z < 3$, our morphological decomposition has also allowed us to investigate how the axial ratio distributions for the passive and star-forming sub-populations of the bulge and disc components differ. The axial ratios of these components have provided another key indicator of the structure of these systems as they reveal that the passive discs have flattened axial ratio distributions consistent with a population of randomly oriented thin discs, similar to discs in the local Universe. This further verifies that these are genuine disc-dominated passive galaxies. However, the star-forming discs have a distribution peaked at higher values of $b/a \sim 0.7$, more consistent with the distributions for the passive and star-forming bulges in this sample, and those for lower redshift bulge-dominated systems.

By exploring the trends within the star-forming disc population, we find evidence that the smallest galaxies are the roundest, and that the most actively star-forming disc galaxies are the flattest. This star-forming–axial ratio trend has also been supported by comparison with a (sub-)mm selected sample. These results are thus consistent with a scenario in which, at high redshift high star formation rates correlate with increased scaleheight of discs (Dekel & Burkert 2014), which affects the axial ratios of the smaller galaxies but has a lesser impact on the larger discs. If there is also a maximal surface density of star formation in high-redshift discs, then the largest, flattest galaxies would also be expected to be the most star-forming, thereby reconciling both of these observations.

## REFERENCES

Allen P. D., Driver S. P., Graham A. W., Cameron E., Liske J., de Propris R., 2006, MNRAS, 371, 2
Baldry I. K., Glazebrook K., Brinkmann J., Ivezić Ž., Lupton R. H., Nichol R. C., Szalay A. S., 2004, ApJ, 600, 681
Bamford S. P. et al., 2009, MNRAS, 393, 1324
Bell E. F. et al., 2012, ApJ, 753, 167
Birnboim Y., Dekel A., 2003, MNRAS, 345, 349

Bluck A. F. L., Mendel J. T., Ellison S. L., Moreno J., Simard L., Patton D. R., Starkenburg E., 2014, MNRAS, 441, 599

Bolzonella M., Miralles J., Pelló R., 2000, A&A, 363, 476

Bournaud F., Elmegreen B. G., Elmegreen D. M., 2007, ApJ, 670, 237

Bournaud F., Dekel A., Teyssier R., Cacciato M., Daddi E., Juneau S., Shankar F., 2011, ApJ, 741, L33

Bournaud F. et al., 2013, ApJ, 780, 57

Bruce V. A. et al., 2012, MNRAS, 427, 1666

Bruce V. A. et al., 2014, MNRAS, preprint (arXiv:1405.5221)

Bruzual G., Charlot S., 2003, MNRAS, 344, 1000

Buitrago F., Trujillo I., Conselice C. J., Bouwens R. J., Dickinson M., Yan H., 2008, ApJ, 687, L61

Buitrago F., Conselice C. J., Epinat B., Bedregal A. G., Grutzbauch R., 2013a, MNRAS, 439, 1494

Buitrago F., Trujillo I., Conselice C. J., Häußler B., 2013b, MNRAS, 428, 1460

Cameron E., Driver S. P., Graham A. W., Liske J., 2009, ApJ, 699, 105

Cameron E., Carollo C. M., Oesch P. A., Bouwens R. J., Illingworth G. D., Trenti M., Labbé I., Magee D., 2011, ApJ, 743, 146

Carollo C. M. et al., 2014, preprint (arXiv:e-prints)

Ceverino D., Dekel A., Bournaud F., 2010, MNRAS, 404, 2151

Chang Y.-Y. et al., 2013a, ApJ, 773, 149

Chang Y.-Y., van der Wel A., Rix H.-W., Wuyts S., Zibetti S., Ramkumar B., Holden B., 2013b, ApJ, 762, 83

Cheung E. et al., 2012, ApJ, 760, 131

Chevance M., Weijmans A.-M., Damjanov I., Abraham R. G., Simard L., van den Bergh S., Caris E., Glazebrook K., 2012, ApJ, 754, L24

Cirasuolo M. et al., 2007, MNRAS, 380, 585

Conselice C. J. et al., 2011, MNRAS, 413, 80

Dahlen T. et al., 2013, ApJ, 775, 93

Davari R., Ho L. C., Peng C. Y., Huang S., 2014, ApJ, 787, 69

de Jong R. S., 1996, A&A, 313, 45

Dekel A., Birnboim Y., 2006, MNRAS, 368, 2

Dekel A., Burkert A., 2014, MNRAS, 438, 1870

Dekel A., Krumholz M. R., 2013, MNRAS, 432, 455

Dekel A. et al., 2009a, Nature, 457, 451

Dekel A., Sari R., Ceverino D., 2009b, ApJ, 703, 785

Driver S. P. et al., 2006, MNRAS, 368, 414

Drory N., Fisher D. B., 2007, ApJ, 664, 640

Elmegreen B. G., Elmegreen D. M., 2005, ApJ, 627, 632

Elmegreen B. G., Elmegreen D. M., Fernandez M. X., Lemonias J. J., 2009, ApJ, 692, 12

Fan L., Fang G., Chen Y., Pan Z., Lv X., Li J., Lin L., Kong X., 2013, ApJ, 771, L40

Fang J. J., Faber S. M., Koo D. C., Dekel A., 2013, ApJ, 776, 63

Förster Schreiber N. M. et al., 2009, ApJ, 706, 1364

Furusawa H. et al., 2008, ApJS, 176, 1

Genzel R. et al., 2011, ApJ, 733, 101

Grogin N. A. et al., 2011, ApJS, 197, 35

Guo Y., Giavalisco M., Ferguson H. C., Cassata P., Koekemoer A. M., 2011, ApJ, 757, 120

Hartley W. G. et al., 2013, MNRAS, 441, 3045

Häussler B. et al., 2007, ApJS, 172, 615

Häußler B. et al., 2013, MNRAS, 430, 330

Holden B. P., van der Wel A., Rix H.-W., Franx M., 2012, ApJ, 749, 96

Hopkins P. F., Kereš D., Murray N., Quataert E., Hernquist L., 2012, MNRAS, 427, 968

Johnston E. J., Aragon-Salamanca A., Merrifield M. R., 2014, MNRAS, 441, 333

Kennicutt R. C., Jr, 1998, ARA&A, 36, 189

Kereš D., Katz N., Weinberg D. H., Davé R., 2005, MNRAS, 363, 2

Koekemoer A. M. et al., 2007, ApJS, 172, 196

Koekemoer A. M. et al., 2011, ApJS, 197, 36

Kormendy J., Kennicutt R. C., Jr, 2004, ARA&A, 42, 603

Krumholz M., Burkert A., 2010, ApJ, 724, 895

Lackner C. N., Gunn J. E., 2012, MNRAS, 421, 2277

Lang P. et al., 2014, ApJ, 788, 11

Law D. R., Steidel C. C., Shapley A. E., Nagy S. R., Reddy N. A., Erb D. K., 2012, ApJ, 745, 85

Lawrence A. et al., 2007, MNRAS, 379, 1599

Lee B. et al., 2013, ApJ, 774, 47

McGrath E. J., Stockton A., Canalizo G., Iye M., Maihara T., 2008, ApJ, 682, 303

McLure R. J. et al., 2013, MNRAS, 428, 1088

Martig M., Bournaud F., Teyssier R., Dekel A., 2009, ApJ, 707, 250

Martig M., Bournaud F., Croton D. J., Dekel A., Teyssier R., 2012, ApJ, 756, 26

Masters K. L. et al., 2010, MNRAS, 405, 783

Michałowski M. J., Dunlop J. S., Cirasuolo M., Hjorth J., Hayward C. C., Watson D., 2012, A&A, 541, A85

Mortlock A. et al., 2013, MNRAS, 433, 1185

Muzzin A. et al., 2013, ApJS, 206, 8

Newman J. A., Davis M., 2002, ApJ, 564, 567

Newman A. B., Ellis R. S., Bundy K., Treu T., 2012, ApJ, 746, 162

Omand C. M. B., Balogh M. L., Poggianti B. M., 2014, MNRAS, 440, 843

Padilla N. D., Strauss M. A., 2008, MNRAS, 388, 1321

Peng C. Y., Ho L. C., Impey C. D., Rix H.-W., 2010a, AJ, 139, 2097

Peng Y.-j. et al., 2010b, ApJ, 721, 193

Ravindranath S. et al., 2006, ApJ, 652, 963

Robertson B., Hernquist L., Cox T. J., Di Matteo T., Hopkins P. F., Martini P., Springel V., 2006, ApJ, 641, 90

Schawinski K. et al., 2014, MNRAS, 440, 889

Scoville N. et al., 2007, ApJS, 172, 1

Sekiguchi K., Akiyama M., Furusawa H., Simpson C., Takata T., Ueda Y., Watson M. W. Sxds Team, 2005, in Renzini A., Bender R., eds, Proc. ESO Workshop, Multiwavelength Mapping of Galaxy Formation and Evolution. Springer-Verlag, Berlin, p. 82

Simard L., Mendel J. T., Patton D. R., Ellison S. L., McConnachie A. W., 2011, ApJS, 196, 11

Skibba R. A. et al., 2009, MNRAS, 399, 966

Stockton A., McGrath E., Canalizo G., Iye M., Maihara T., 2008, ApJ, 672, 146

Talia M., Cimatti A., Mignoli M., Pozzetti L., Renzini A., Kurk J., Halliday C., 2013, A&A, 562, 113

Targett T. A. et al., 2013, MNRAS, 432, 2012

Trump J. R. et al., 2009, ApJ, 696, 1195

van der Wel A. et al., 2011, ApJ, 730, 38

van der Wel A. et al., 2012, ApJS, 203, 24

Vika M., Bamford S. P., Haeussler B., Rojas A. L., Borch A., Nichol R. C., 2013, MNRAS, 435, 623

Wang T. et al., 2012, ApJ, 752, 134

Williams R. J., Quadri R. F., Franx M., van Dokkum P., Labbé I., 2009, ApJ, 691, 1879

Wuyts S. et al., 2011, ApJ, 738, 106

Wuyts S. et al., 2012, ApJ, 753, 114

# APPENDIX A: MULTIPLE-COMPONENT FITTING

For this analysis, we have adopted multiwavelength decompositions which are based on the best-fitting model parameters of the $H_{160}$-band fits, with all model parameters fixed at other wavelengths except for the magnitude of each component. Several tests of the validity of this approach have been conducted by also allowing the effective radii and axial ratios of the components to be included as free parameters in the fitting and we have explored how these affect not only the $\chi^2$ statistics of the fits, but also the output bulge and disc magnitude contributions and fitted sizes.

The first tests conducted were to study how the introduction of the additional free parameters influenced the acceptability of the best-fitting models. While allowing the effective radii ($r_e$) and axial ratios ($b/a$) parameters to be freely fitted in the modelling did, unsurprisingly, provide appreciable improvement in the $\chi^2$ fits for a few of the objects in the sample (Fig. A1), we found evidence that there is the potential for significant biases to be introduced as a consequence of adopting the increased degrees of freedom. Moreover,
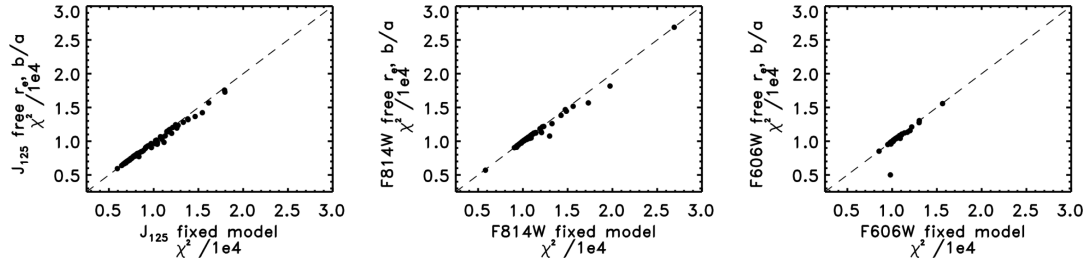
**Figure A1.** Comparison of the minimum $\chi^2$ between the fixed $r_e$ and $b/a$, and the free $r_e$ and $b/a$ model fits. Left: comparison in the $J_{125}$ band, middle: for the $i_{814}$ band, right: for the $v_{606}$ band. These comparisons illustrate that the additional degrees of freedom introduced by allowing the $r_e$ and $b/a$ parameters to be freely fitted significantly improve the fits for only a small sub-set of the galaxies in our sample.
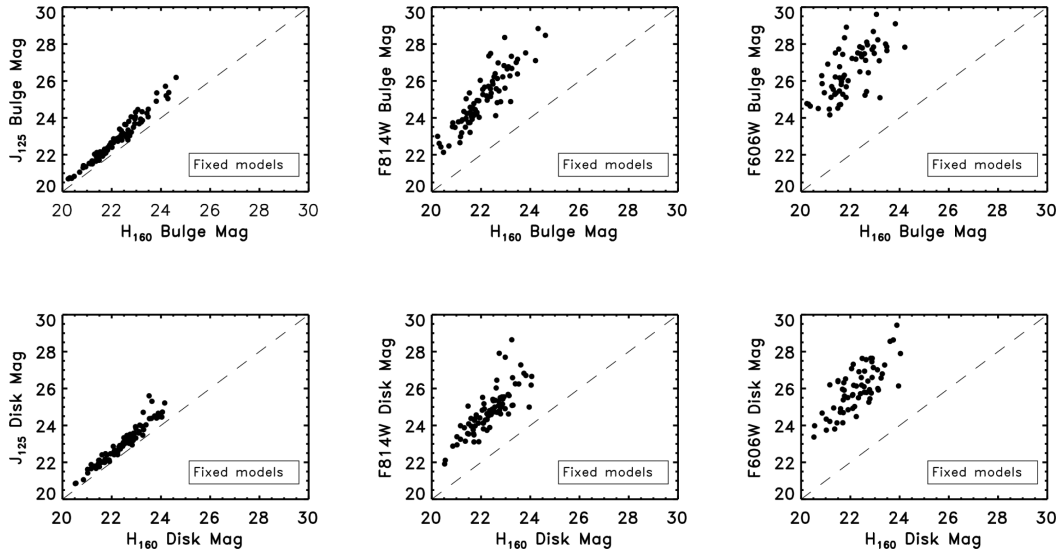


**Figure A2.** Comparison of the fitted magnitudes of the fixed parameter multiwavelength models for the separate bulge and disc components in relation to the $H_{160}$ model fits. The top panels show the comparison between the magnitudes of the bulge components across the additional three bands and the original $H_{160}$ model fits, and the bottom panels illustrate this comparison for the disc components.

when comparing the bulge and disc component magnitudes in all bands it is clear that in both cases, where $r_e$ and $b/a$ are held fixed (Fig. A2) and allowed to fit freely (Fig. A3), the overall trend for the magnitude of both components to become fainter than the $H_{160}$ estimates remains, with the introduction of only additional scatter to this relation for the case where the $r_e$ and $b/a$ parameters are fitted freely.

Furthermore, from examining the total multiple-component (bulge+disc and bulge+disc+PSF) magnitudes of each component from both the fixed and free $r_e$ and $b/a$ parameter models, we found that towards the bluer wavelengths, the scatter in the relation between this integrated measure of the total magnitude of the object and the isomagnitude estimate, measured directly from the image, increases in the case of the free $r_e$ and $b/a$ fits. This is demonstrated in Fig. A4, where it can also be seen that this increase in scatter is preferentially in the direction of the total multiple-component magnitude being brighter than the measured isomagnitude.

In addition to this, a comparison of the bulge and disc sizes of each component in the four different bands revealed that by allowing the effective radius and axial ratio to be free parameters, the scatter in the relation between the effective radius of each component in the given bands compared to the master fit from the $H_{160}$ band (Fig. A5) also increases, and highlights clear cases where in the $v_{606}$ band, the

bluest available, the bulge component becomes significantly larger than in the $H_{160}$ band. These trends suggest that introducing the effective radius and axial ratio as free parameters, and removing the $H_{160}$ band constraints on these parameters, introduces new biases in the fitting procedure which, while hard to correctly interpret, do not significantly improve the ability of the models to reproduce the underlying morphologies of the galaxies in our sample. Moreover, this also holds true for the case of objects which were modelled as pure bulges in the $H_{160}$ band, and where we have added an additional $n = 1$ disc component in the bluer bands (where for this additional disc model all other parameters except for the centroid position and Sérsic index were allowed to vary).

For these objects, the addition of the second component to account for any faint discs becoming dominant in bluer bands still did not provide a significant improvement in the ability of the model to fit the data, and due to low number statistics, it is hard to argue from examining the fraction of light which becomes attributed to the disc in the $v_{606}$ band compared to the $H_{160}$ band that the addition of such a disc component is motivated.

In conclusion, we decided to adopt fixed $r_e$ and $b/a$ parameter models for the multiwavelength morphological analysis in order to avoid adopting additional degrees of freedom, which are not required and may introduce an additional degree of bias.
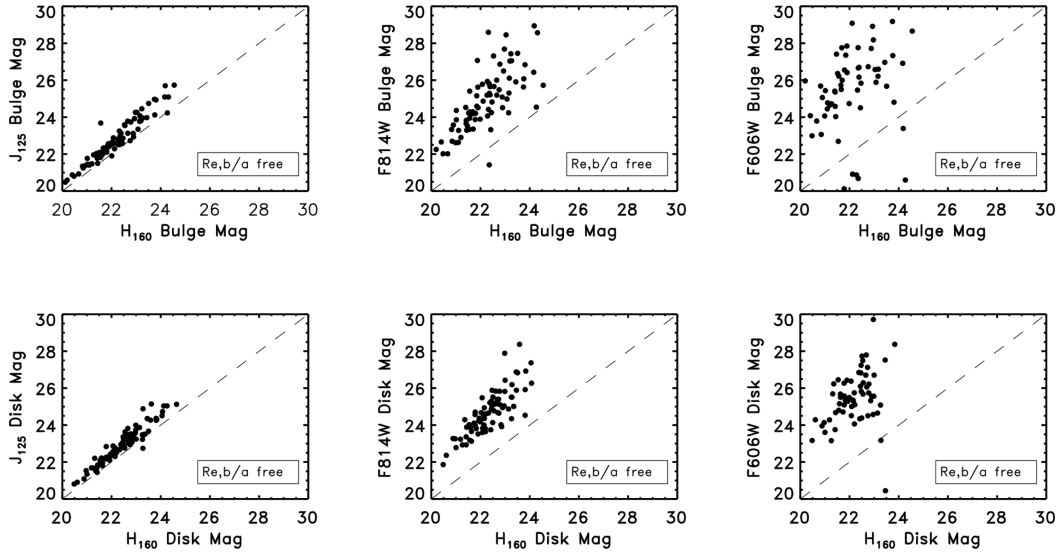
**Figure A3.** The fitted magnitudes of the free parameter multiwavelength models for the separate bulge and disc components in relation to the $H_{160}$ model fits. The panels follow the same configuration as in Fig. A2, with the comparison for the bulge components in the top panels and the discs in the bottom panels.
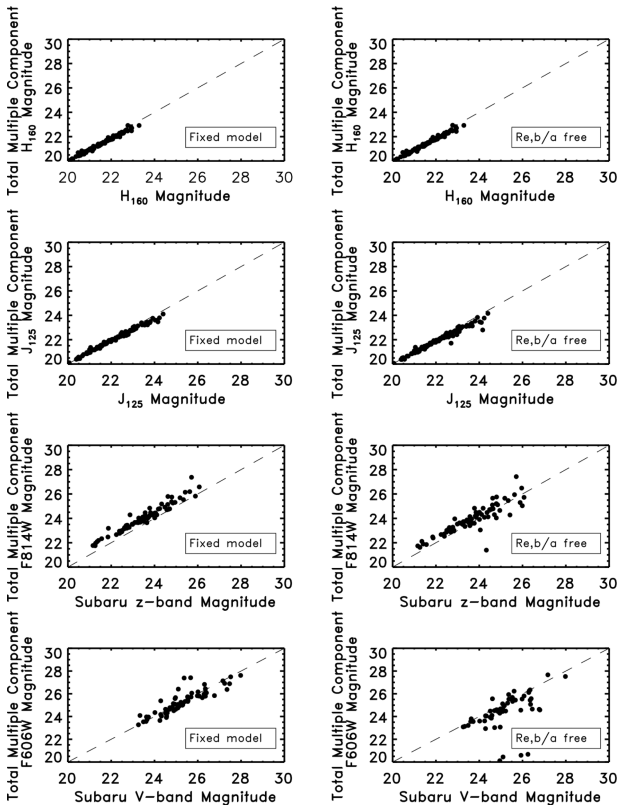


**Figure A4.** Relation between the sum of the best-fitting multiple-component model magnitudes and the measured isomagnitude of each object for the fixed and free $r_e$ and $b/a$ parameter models. The fixed parameter models are shown on the left, with the free parameter models on the right, and the plots are ranked from top to bottom by decreasing wavelength. The constant offset between the best-fitting modelled $z_{814}$-band magnitudes and the measured Subaru $z$-band magnitudes is due to the mismatch in the central wavelengths of these filters. These plots illustrate how the adoption of the additional free parameters results in some case where the sum of the best-fitting bulge+disc model magnitudes exceeds the measured isomagnitude photometry and so demonstrates that this extra freedom can result in biases in the fitting which are hard to understand.

Further example fits of representative objects across all four of the CANDELS bands are given in Figs A6–A9.

## APPENDIX B: DOUBLE-COMPONENT SED FITTING

Further to the example given in Fig. 3, additional double-component SED fits for objects with $H_{160}$-band best-fitting morphologies with $B/T \sim 0.5$ and $B/T > 0.5$ are given here, to further illustrate how well the model photometry is fitted using the fixed $H_{160}$ parameter model approach with the extension to additional ground-based $\lambda < 0.6\,\mu m$ and $\lambda > 1.6\,\mu m$ data with re-measured 2.5 arcsec aperture photometry in the blue bands.

## APPENDIX C: BEST-FITTING SED TEMPLATES

The extra degrees of freedom introduced by the bulge+disc models also help to mitigate the need for limitations on the star formation history templates and allowed ages of the models considered during the SED fitting. Having conducted several tests for different sub-sets of star formation histories, we find that there is no longer any need to restrict either component to a minimum age of $>50\,Myr$ or to exponentially star formation histories in the range $0.3 \leq \tau\,(Gyr) \leq 5$, as a second younger burst, or exponentially decaying star-forming population can reasonably account for any continued or recent star formation superimposed on an older, redder population.

In fact, in the 56 cases where the best-fitting two-component models are double-burst models, 53 galaxies have at least one component with an age of $>50\,Myr$ and 49 galaxies have at least one component with an age of $>500\,Myr$, which we use to provide a more robust measure of passivity. This trend also extends to the double-$\tau$ and burst+$\tau$ models, where none of the fits have both components with ages $<500\,Myr$. Moreover, for the double-burst models there are only 21/56 objects where both components are older than 500 Myr and the SED fits to the photometry find no evidence for ongoing star formation. The agreement between the ages of the old component from the full $0 \leq \tau\,(Gyr) \leq 5$ double-component models and the
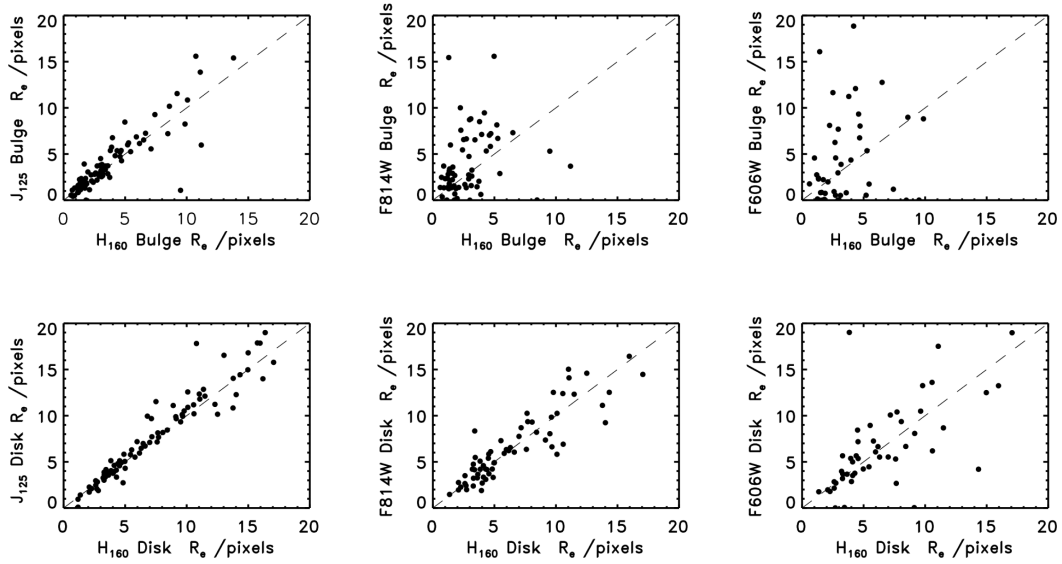
**Figure A5.** Comparison of the fitted sizes of the individual components between the fixed and free-parameter models for the four bands. These plots illustrate that allowing the $r_e$ and $b/a$ parameters to be fitted freely, even in the bluest band ($v_{606}$), results in cases where the disc component becomes both larger and smaller compared to the master $H_{160}$-band fit, and, moreover, highlights cases where in the $v_{606}$ band the bulge size exceeds the fitted sizes in the redder bands.
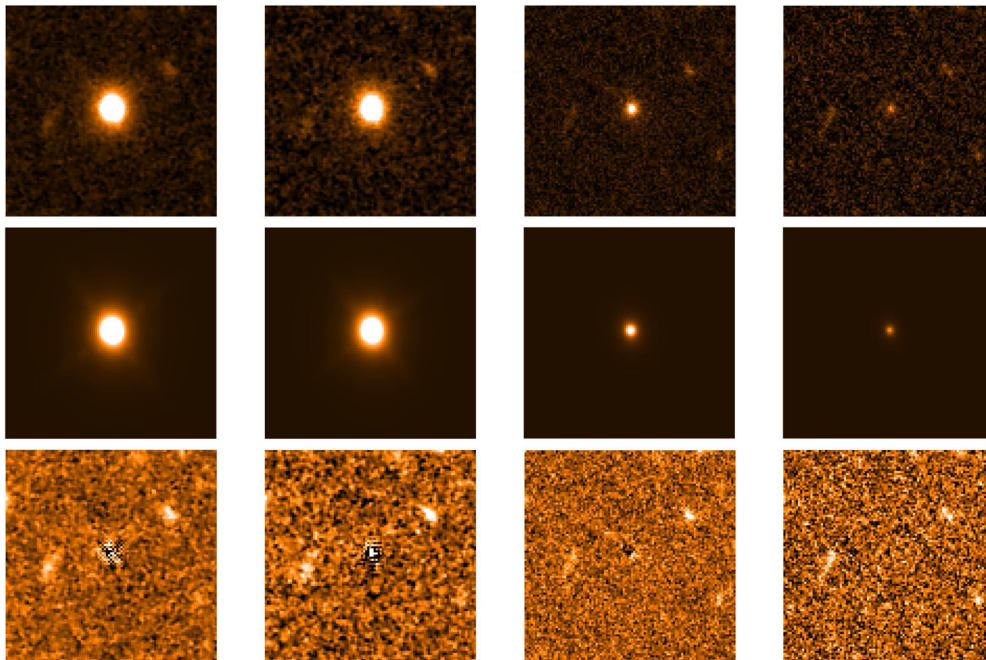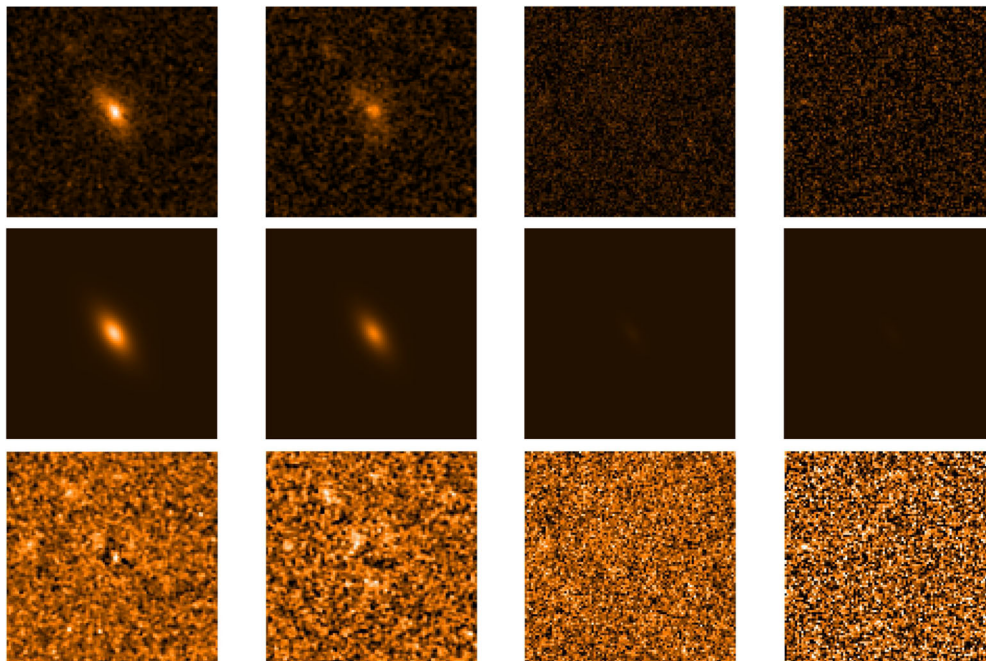


**Figure A6.** Image stamps of an example fit for a pure-bulge object. The images displayed are $6 \times 6$ arcsec stamps with the images in the top panels, the best-fitting models in the middle panels and the residual stamps in the bottom panels. The columns are ranked from left to right by decreasing wavelength, with the $H_{160}$-band stamps on the far-left, then the $J_{125}$-band stamps, the $i_{814}$-band stamps and the $v_{606}$-band stamps on the far-right. This is a representative fit for an object which is best fitted with a pure bulge model, and illustrates the level of fits achieved across the full wavelength range in this study by fixing all model parameters, except magnitudes, to the $H_{160}$-band fits.

ages of the single populations from the original single component, limited $0.3 \leq \tau \, (\mathrm{Gyr}) \leq 5$ and age capped, SED fitting is shown in Fig. C1.

As a secondary check, the ages of these double-burst fits for objects which have 24 µm counterparts from SpUDS and S-COSMOS have also been examined and are consistent with the fitting in that, for these double-burst models, there is always a young component which can account for star formation and none of the galaxies with

24 µm counterparts have both components with ages >500 Myr, as can be seen in Fig. C2.

As an additional check of this approach, it can also be seen from Fig. C2 that our adoption of the 500 Myr age boundary (above which we attribute none of the entire galaxy's star formation to the component) is justified as there is no additional evidence from 24 µm of on-going star formation in these components with older ages.
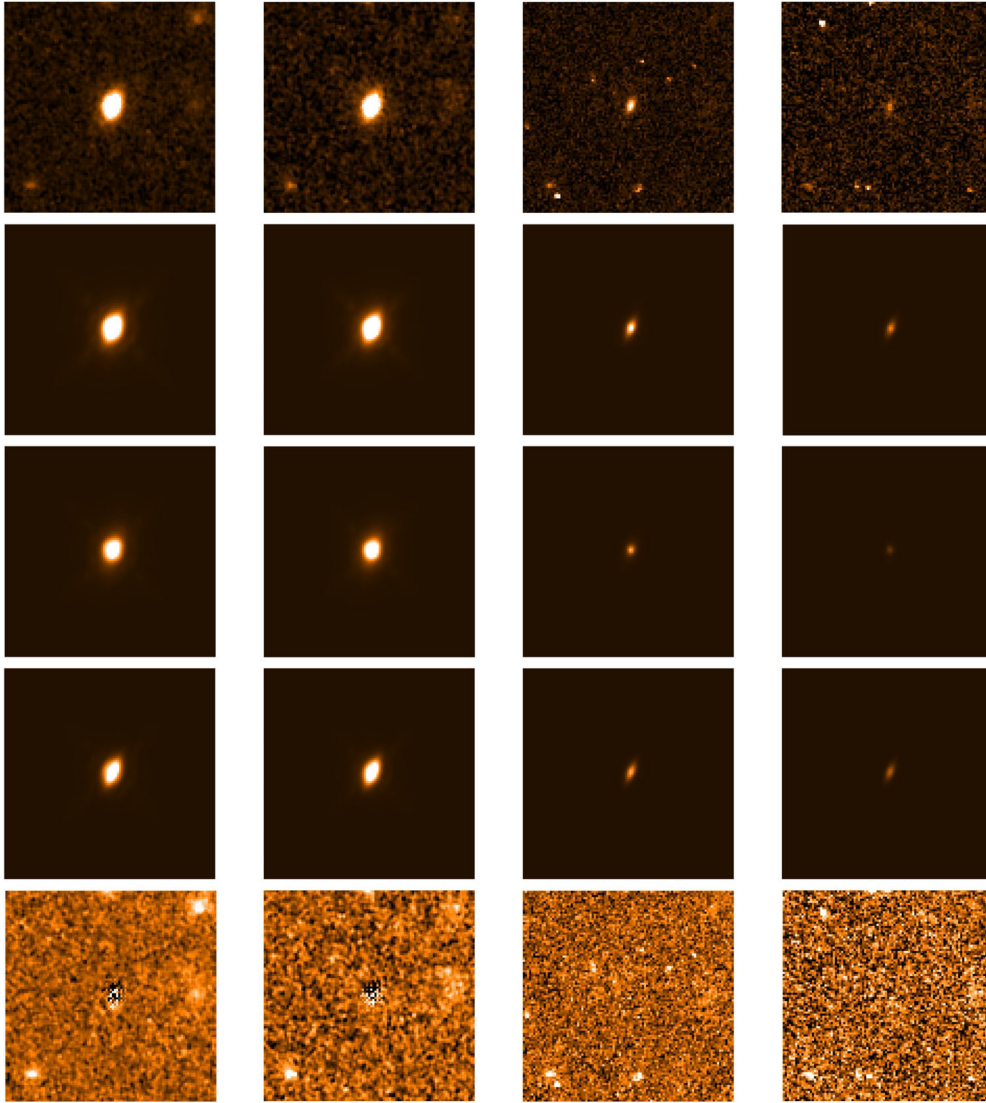
**Figure A7.** Image stamps of an example fit for a pure-disc object. As in Fig. A6, displayed are 6 × 6 arcsec image, model and residual stamps, ranked from left to right by decreasing wavelength. In this case, the image and model stamps from this fitting clearly illustrate that, despite being best fitted by a pure-disc morphology, this component becomes fainter in the bluer bands. The residuals show that no additional structure becomes prominent at the bluer wavelengths.
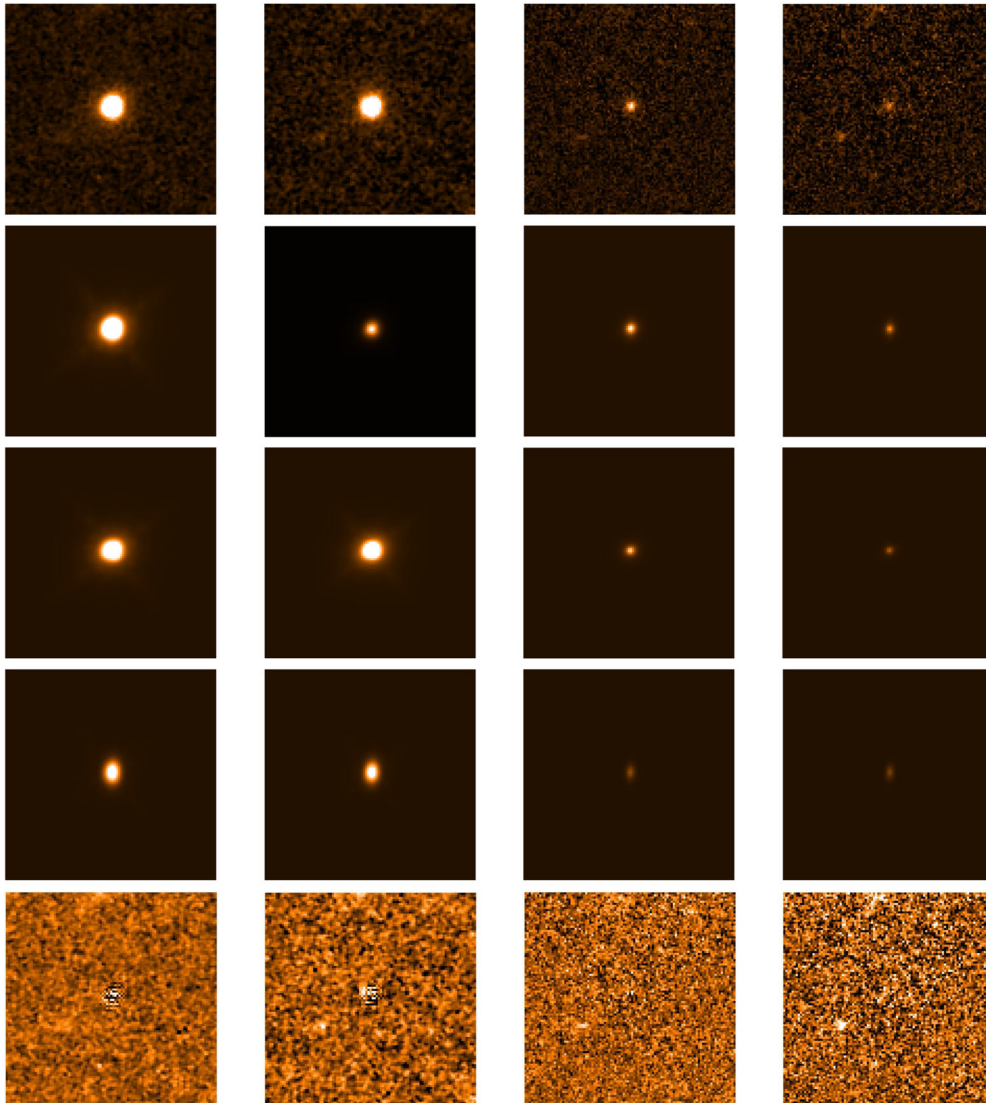
**Figure A8.** Image stamps of an example fit for a bulge+disc object with $D/T < 0.5$. The configuration of these stamps is as follows. Left to right: $H_{160}$, $J_{125}$, $i_{814}$ and $v_{606}$. Top to bottom: images, best-fitting combined bulge+disc models, individual best-fitting bulge components, individual best-fitting disc components and combined model residuals. In comparison to Fig. 2, for this object the disc is the dominant component, although it can also be seen that the bulge component remains prominent even in the $v_{606}$ band.

**Figure A9.** Image stamps of an example fit for a bulge+disc object with $B/T = 0.5$, again following the placement of stamps described in the caption of Fig. A8. This object has a more equal contribution from the bulge and disc components. As with the previous examples, examination of the residual stamps for all four bands illustrates the good quality of the fits achieved by the adopted modelling technique, with no evidence of any additional structure in the bluer bands which has failed to be reproduced by the best-fitting models.
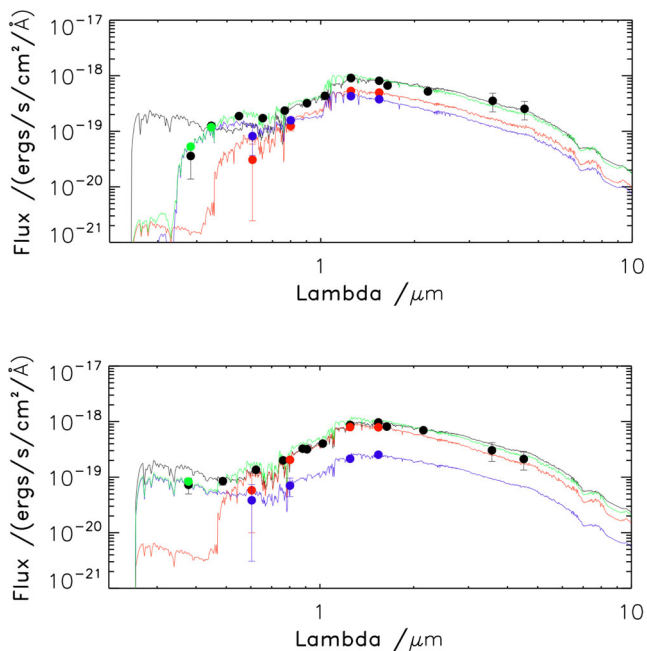
**Figure B1.** SED fits for the example objects shown in Figs A9 and A8, respectively. Top panel for the $B/T \sim 0.5$ fit, and bottom panel for the $B/T > 0.5$ object. Plotted as black data points and the solid black line is the total, overall galaxy photometry (with its associated error bars) and the corresponding best-fitting single-component SED. In blue is the modelled disc component photometry and the corresponding best-fitting decomposed disc SED model, and in red is the modelled bulge photometry and the best-fitting decomposed bulge SED model. Overplotted in green is the sum of the best-fitting bulge and disc SED models, which can be directly compared to the single-component fit in black and can be seen to be in better agreement with the overall galaxy photometry. Finally, the green points, and their error bars, are the re-measured 2.5 arcsec radius photometry for the blue bands. The top panel shows the fits to an object from the COSMOS field, where only $u'$-band photometry is available, whereas the bottom panel shows an object from the UDS field with re-measured photometry for both the $u'$ and $B$ bands.
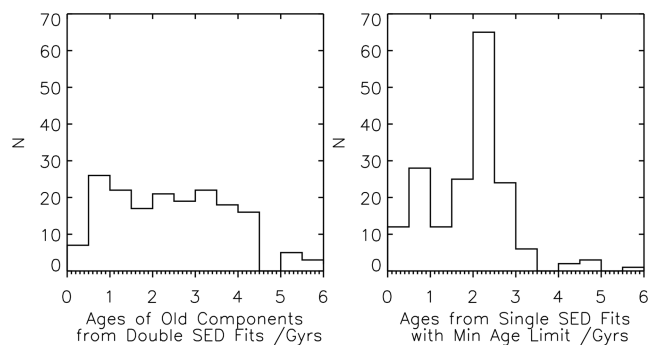


**Figure C1.** Comparison between the age distributions of the single-component models and the older components of the double-component models. Left: the age distribution of the old component of double $0 \leq \tau$ (Gyr) $\leq 5$ models. Right: distribution of the ages from single, limited $0.3 \leq \tau$ (Gyr) $\leq 5$ and age-capped SED fits. The rough agreement between these distributions at the very youngest age bins ($<1$Gyr) verifies that the additional degrees of freedom introduced by the double $0 \leq \tau$ (Gyr) $\leq 5$ models naturally resolve the problem encountered with single SED fits sometimes becoming restricted to un-physically young ages.
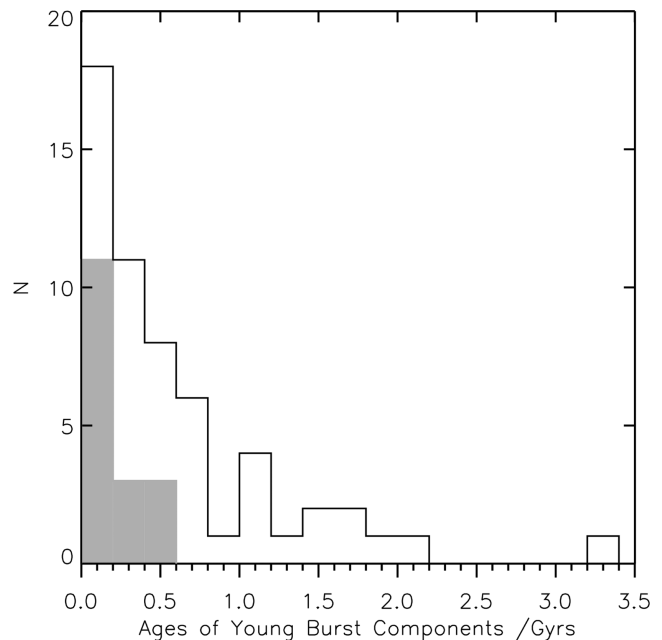


**Figure C2.** Age distribution of the young components of the double-burst fits, overplotted by the shaded region with the objects which were found to have a 24 μm counterpart. The lack of objects with 24 μm counterparts and ages $>500$ Myr confirms that the 500 Myr criterion for passivity is physically motivated, and that the double-burst models produce realistic ages and star formation rates for the massive galaxies in our sample.

This paper has been typeset from a TEX/LATEX file prepared by the author.